ATOMISTIC SIMULATIONS FOR COMPUTING SOLID LIQUID INTERFACE PROPERTIES OF THE Al-Mg SYSTEM

ATOMISTIC SIMULATIONS FOR COMPUTING SOLID LIQUID INTERFACE PROPERTIES OF THE Al-Mg SYSTEM

By

MD. JAHIDUR RAHMAN, B. Eng.

A Thesis

Submitted to the School of Graduate Studies

In Partial Fulfilment of the Requirements

for the Degree

Master of Applied Science

McMaster University

MASTER OF APPLIED SCIENCE (2009) McMaster University

(Materials Science and Engineering) Hamilton, Ontario

TITLE:	Atomistic Simulations for computing solid liquid interface properties of the Al-Mg system
AUTHOR:	Md. Jahidur Rahman, B. Eng. (Bangladesh University of Engineering and Technology, Bangladesh)
SUPERVISOR:	Dr. Jeffrey J. Hoyt
NUMBER OF PAGES:	xviii, 92

Abstract

Crystal-melt interface properties and their associated anisotropies play a crucial role during solidification in controlling the nucleation, crystallization rate and growth morphology. There are two solid-liquid interfacial (SLI) properties affecting the dendritic microstructures that form in the crystallization process and the SLI properties are interfacial free energy (γ) and kinetic coefficient (μ). In this research work, atomic scale simulation techniques, such as Monte Carlo (MC) and Molecular Dynamics (MD), have been applied to compute the crystal-melt interface properties and their anisotropies of the Al-Mg system.

An inter-atomic potential is utilized for describing the pair interactions of binary Al-Mg system during atomistic simulations. Actually the potential was developed particularly for the simulation of solid-liquid interface properties of Al-Mg alloys. Optimization of the potential is conducted by determining the equilibrium phase diagram employing Monte Carlo (MC) simulation techniques and comparing with the experimental results. A method is discussed for fitting the potential into phase diagram by varying the data for liquid solution energies. A good agreement of the Al-rich side of Al-Mg phase diagram, determined from this potential, is found with the experimental phase diagram. The inter-atomic potential is also optimized by comparing the liquid enthalpy of mixing of Al-Mg alloys with that of experiments.

The crystal-melt interfacial energy (γ) and its anisotropies in Al-Mg binary alloys are computed utilizing a combination of MC and MD simulations in association with the analysis of capillary fluctuation method (CFM). The orientation averaged surface energy γ_0 is observed to increase with increasing temperature which is consistent with other computational results of Lennard Jonnes (LJ) and Hard Sphere (HS) system. The anisotropy of γ is found to follow the ordering of $\gamma_{100} > \gamma_{110} > \gamma_{111}$. Superimposition of the γ anisotropy parameters on the orientation selection map, proposed by Haximali *et al.*, predicts the primary dendrite growth in <100> direction for pure Al and the growth is examined to be stabilized in the same orientation with the addition of Mg atoms to Al i.e. in the concentrated alloys as well.

Kinetic coefficient (μ) of pure Al is determined from the free solidification method utilizing Molecular Dynamics (MD) simulations employing multiple thermostats in the system which avoids the underestimation of μ due to slow dissipation of the generated latent heat at the solid-liquid interface. Kinetic coefficient is also extracted from equilibrium fluctuation analysis with a correction due to the contribution of thermally controlled interfacial kinetics. μ is computed for both (100) and (110) orientations of the crystal-melt interfaces and the values from both techniques are found to be equivalent. The magnitudes of interface mobility for pure Al is determined as μ_{100} = 163 cm/s/K and μ_{110} = 129 cm/s/K.

Acknowledgement

MJR would like to express his heart depth gratitude to his supervisor Dr. Jeffrey J. Hoyt for his continuous guidance, constructive suggestions and useful instructions to this research work. I am also indebted to him for introducing me into such an interesting atomistic research arena of computer simulation which is a great privilege for me. The author is pleased to thank Mikhail Mendelev from Ames Laboratory and Mark Asta from University of California at Davis for their technical assistance, cooperative conversations over the course of this study. A special note of thanks will go to Alain Karma from North Eastern University for the helpful discussions with him. The U.S. Department of Energy (DOE) sponsored Computational Materials Science Network (CMSN) program is also acknowledged for facilitating the collaboration with its associates.

This research work was financially supported by a Natural Sciences and Engineering Research Council of Canada (NSERC) Discovery grant. The author would also like to gratefully acknowledge Shared Hierarchical Academic Research Computing Network (SHARCNET) for providing its high performance computing resources to facilitate this research work.

Throughout the work of this project author has benefited a lot from enlightened conversations with the research group of Dr. Hoyt on several topics herein discussed. At this point I want to admit the weekly group meetings with my supervisor and his group which were very productive and provided me many helpful inputs. I would also like to

appreciate the assistance of laboratory manager Ed McCaffery of MSE department, McMaster University regarding all kinds of computer related technical problem. I am really thankful to my fellow graduate friends for their great company.

At last but not the least, I wish to express my sincere gratitude to my parents for their eternal love, patience and endless support to me. Their souls and shadows were always with me at each and every step of my life and their inspirations support me a lot for my success.

Table of Contents

List of Figures

Chapter – 1

Chapter – 2

Chapter – 3

Chapter – 4

Chapter – 5

List of Tables

List of Symbols

α	A parameter which is tuned to obtain better Al-Mg phase diagram
$\Gamma_{Mg}^{(Al)}$	Adsorption coefficient of Mg with respect to Al
$\Gamma_{AL}^{(Mg)}$	Adsorption coefficient of Al with respect to Mg
θ	Angle between the growth direction and interface normal
ε_1	Anisotropy parameter of interfacial energy for four fold symmetry
ε_2	Anisotropy parameter of interfacial energy for six fold symmetry
ρ_{Al}^{s}	Atom density of Al for the bulk solid phase
ρ_{Al}^{l}	Atom density of Al for the bulk liquid phase
ρ_{Mg}^{s}	Atom density of Mg for the bulk solid phase
ρ_{Mg}^{l}	Atom density of Mg for the bulk liquid phase
$\vec{r}_{fcc}$	Atom position at the ideal fcc sites
$A(k,0)$	Reference amplitude at some arbitrary time
k_B	Boltzmann constant
Γ	Capillary length
μ_{Mg}	Chemical potential of Mg
μ_{Al}	Chemical potential of Al
$\Delta\mu$	Chemical potential difference between Mg and Al

C_{Mg}	Composition of Mg
T_c	Critical temperature below which the miscibility gap exists
a	Cross sectional area of the simulation cell
H^S	Enthalpy of the solid phase
H^L	Enthalpy of the liquid phase
ΔH_M	Enthalpy of mixing for the liquid phase
H_{Al}	Enthalpy of pure Al
H_{Mg}	Enthalpy of pure Mg
$A(k)$	Fourier transform of the amplitude of interface fluctuation
G^S	Gibbs free energy of the solid phase
G^L	Gibbs free energy of the liquid phase
Ω	Grand potential
$\vec{r}_i$	Neighbouring atom position of a fcc atom
S_{xs}	Interfacial excess entropy
γ	Interfacial free energy
V	Interface growth velocity
$\hat{n}$	Interface normal
f	Interface stress
T_I	Interface temperature
ΔT	Interface under-cooling

$\gamma + \gamma''$	Interfacial stiffness
d_{ijk}	Inter planar spacing of (*ijk*) orientation
μ	Kinetic coefficient
L	Latent heat of melting of pure Al
L^s	Lattice parameter of crystal fcc
x^l_{Mg}	Liquidus composition in terms of Mg concentration
T_M	Melting point of pure Al
N_{Al}	Number of Al atoms
N_{Mg}	Number of Mg atoms
ϕ	Order parameter which locates the interface position
γ_0	Orientation averaged interfacial free energy
E_l	Potential energy per atom of the liquid phase
E_s	Potential energy per atom of the solid phase
R_i	Radii of curvature
τ	Relaxation time of the interface fluctuation
τ_1	Relaxation time due to heat flow contribution
x^s_{Mg}	Solidus composition in terms of Mg concentration
K	Thermal conductivity
D_T	Thermal diffusivity

$\left\langle \frac{\partial T}{\partial z} \right\rangle$	Thermal gradient due applied heat flux
N_T	Total number of atoms
$\dot{E}$	Slope of the potential energy per atom vs. time curve
S	Stiffness of the (100)[010] oriented interface
S_{xx}	Stiffness of the (110)[1 $\bar{1}$ 0] oriented interface
S_{yy}	Stiffness of the (110)[001] oriented interface
ΔT	Under-cooling applied in the system
V_s	Volume per atom of the bulk crystal phase (fcc)
k	Wave vector of the interface fluctuation

CHAPTER 1

Introduction

1.1 Importance of Al-Mg Alloys

Pure aluminum has been used in the automotive industries to meet the requirements of the savings of fuel consumption due to reduction in weight. The resistance to corrosion provided by aluminum takes a new importance which leads the automakers to offer longer warranties against body rust-out and component failure. Aluminum bodies have been designed for the delivery vans of U.S. Postal Service for the last 24 years[1]. Actually the application of automotive aluminum is growing over the years both in absolute quantity per car and as a percentage of vehicle weight. In a study by The Aluminum Association Inc. [2001][1], it was found that in 1960, the average aluminum content of the U.S. car was nearly 54 pounds containing 1.4 percent of its total weight which had climbed up to around 250 pounds or about 8 percent of total weight after 27 years. Another study by Miller [2000] reports that the use of aluminum has increased 80% from 1996 to 2000 and is expected up to 300% by 2015.

Alloying additions to Al is very important to improve the mechanical properties, as pure Al is not suitable in almost all cases because of its lower strength. Magnesium is

one of the most effective and widely used alloying elements for auto aluminum and is the principal element in the 5xxx series alloys. Most of the commercial alloys contain magnesium ranging all the way from 0.5 wt% to ~ 6 wt% Mg combined with some iron, chromium, silicon, copper, manganese and zinc. Other elements are present only in small amounts such that their effect on physical properties of the alloys is submerged by that of magnesium. Al-Mg alloys are of great interest in commercial uses as they provide high

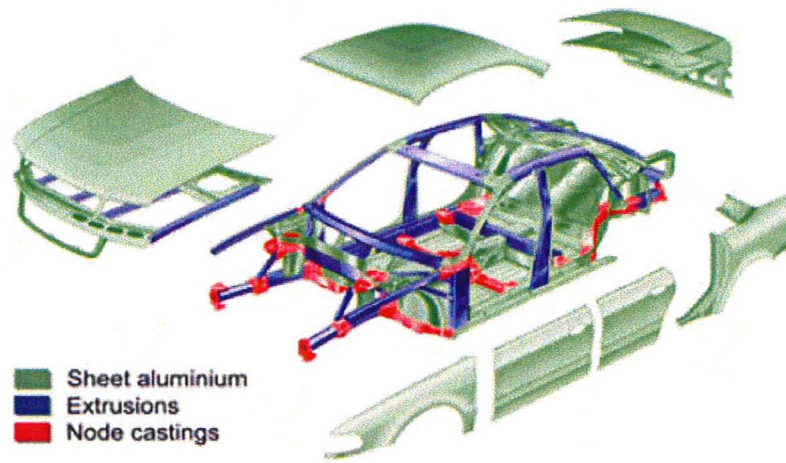

Fig. 1.1: Use of Al-alloys in the automotive parts of Audi – A8 (courtesy to master's thesis of Sanjay Kumar Vajpai) [http://www.keytometals.com]

strength with a wide range of ductility. These alloys provide high formability and durability and with high Mg content they show good cast-ability. Al-Mg alloys are readily weldable and have excellent resistance to corrosion, even in marine environments and salt-water sensitive shore applications. The combination of such mechanical properties makes these alloy potential candidates for automotive and aerospace applications. The recyclability of these alloys also provides both economic and environmental benefits. The

major applications of Al-Mg alloys in the automotive industries include interior body panels and components, splash guards, heat shields, air cleaner trays and covers, structural and weldable parts, load floors (sheets) and engine accessory brackets and mounts[2]. In Fig. 1.1, the general uses of Al-alloys in automotive parts are shown for the Audi – A8.

1.2 The Cast Al-Mg Alloys and Their Morphologies

Casting processes receive a great deal of attention as the conventional production method of commercial Al-Mg alloys due to the low melting point of these alloys and their good castability. Generally during casting, solidification starts with the aluminum as primary crystals that grow as dendrites while the other constituents segregate at the grain boundaries or between the dendrite arms. Actually the dendrites are branched tree like morphologies which propagate into the liquid throughout the course of solidification from the melt. The mechanical integrity of these cast alloys critically depends on the complex morphology of dendritic microstructures as they control the material properties to a great extent. Such a dendritic morphology is shown in Fig. 1.2 which illustrates the snowflake pattern formation of the dendrites.

A large number of studies have been conducted over the years for the development of a theoretical understanding of dendritic solidification. An important advancement was the advent the of microscopic solvability theory of steady state dendrite

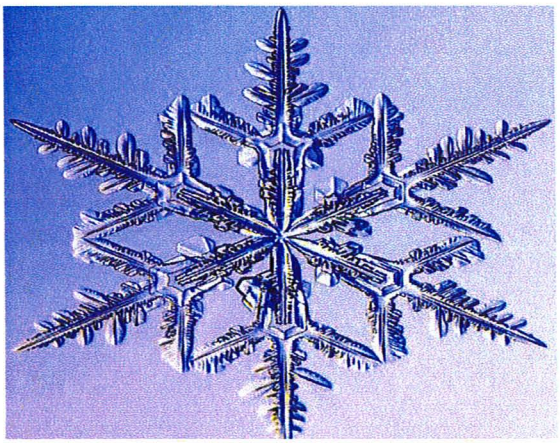

Fig. 1.2: Formation of snowflakes dendritic morphology during solidification[3]

growth[4-7], which predicts that the crystalline anisotropy plays a crucial role in determining the growth rate and tip radius of dendrites. The formation of a branched pattern morphology of the dendrites strongly depends on the anisotropy of the solid-liquid interfacial free energy and on the magnitude of anisotropy of the interface mobility as well at higher growth velocities. The main predictions of the solvability theory have been validated by several recent phase field simulation[8-14] studies.

1.3 Crystal-Melt Interface Properties

There are two solid-liquid interfacial (SLI) properties that control the crystallization rate and growth morphology of dendrites: kinetic coefficient (μ) is defined to be the constant of proportionality between the growth velocity and interface undercooling, and the interfacial free energy (γ) is the free energy required per unit area to create an interface between the crystal and its own melt. The orientation dependence of

these SLI properties causes the instability of planar interface leading to the formation of dendrites. This phenomenon is resulted from the variation in interface temperature with change in the magnitude of μ and γ due to their anisotropy. According to the velocity dependent Gibbs–Thompson condition, the temperature at any point along the crystal-melt interface during solidification can be expressed as[15]:

$$T_I = T_M - \frac{T_M}{L}\sum_{i=1,2}\left[\gamma(\hat{n}) + \frac{\partial^2\gamma(\hat{n})}{\partial\theta_i^2}\right]\frac{1}{R_i} - \frac{V_n}{\mu(\hat{n})} \qquad (1.1)$$

where, T_M is the melting temperature, L is the latent heat of melting per unit volume, $\gamma(\hat{n})$ is the anisotropic interfacial free energy while $\hat{n}$ represents the normal vector to the growth direction, θ_i refers to the angle between the growth direction and $\hat{n}$, R_i is the principal radii of curvature, V_n is the normal velocity of interface growth and $\mu(\hat{n})$ is the anisotropic kinetic coefficient. The second term represents the lowering of the local melting point due to the curvature and the third term comes from the effect of the kinetic undercooling. Eq. 1.1 shows that the interface temperature will vary due to the orientation dependence of $\gamma(\hat{n})$ and $\mu(\hat{n})$. This will cause a lowering of the interface temperature in some certain direction more than that of other directions and this will trigger the crystal to grow rapidly in that direction to form a dendritic structure. For this reason, the anisotropy of the solid-liquid interface is very important for the formation of the dendrite during crystallization. If the anisotropy is not considered, the crystal will grow by same extent in all direction and hence no dendrites would be observed.

1.4 Role of Crystalline Anisotropies in Controlling Dendrite Growth Direction

In the last two decades, the phase field approach has emerged as an effective method for the modelling dendritic evolution; starting from solidification of pure materials[16-17] and extended to alloy systems[10,18] later on. Simultaneously, several atomistic simulations such as Molecular Dynamics (MD) and Monte Carlo (MC) simulation methods have been developed to compute accurately the crystal-melt interfacial properties and their associated anisotropies[15,19-27]. Among the atomic scale MD simulation techniques that have emerged for the determination of solid-liquid interfacial free energy, the Capillary Fluctuation Method (CFM), introduced by Hoyt et al.[20], described a comprehensive technique for computing the anisotropy of the interfacial energy with high statistical precision which leads to a better prediction of the morphological variation of dendritic microstructures during solidification. This method is based on the analysis of MD measurements of equilibrium height fluctuations of the solid-liquid interface to extract the interface stiffness, defined as $\gamma + \gamma''$ where γ is the interfacial free energy and γ'' is its second derivative with respect to orientation. Actually stiffness is calculated as this quantity can vary significantly as a function of orientation and will largely control the interface fluctuation. The anisotropy of interfacial energy is known to be small, on the order of 1–2%[28-29], for the rough crystal-melt interfaces in metals but stiffness is one order more anisotropic than γ itself. Applications of CFM for the studies of interfacial free energies in elemental Ni[20] , Au[21], Ag[21], Pb[19], Cu[19] and Al[30], as well as the model systems Lennard-Jones[31] and Hard-Sphere[32] have shown

that two anisotropy parameters, a fourfold and a sixfold anisotropy denoted by ε_1 and ε_2 respectively, are required to capture accurately the entire orientation dependence of interfacial energy and hence the dendrite growth directions. Previous theoretical and numerical studies of dendrite growth have assumed a single anisotropy parameter with positive ε_1 and the higher order anisotropic parameter ε_2 was assumed to be negligibly small [8-12].

In alloy dendritic solidification, numerous experimental investigations have concluded that the composition variation can alter the crystalline direction of growth of a dendrite[33-39]. The solute induced changes in the growth morphologies have encapsulated wide range of applications to optimize the material behaviour by controlling the dendritic microstructures. In a classic study of this phenomenon, Haxhimali et al.[33] have shown, both computationally and experimentally in Al-Zn alloys, that dendritic growth exhibits a continuous change of direction from <100> to <110> as the solute (Zn) is added to the system. The authors explain the change in orientation selection in terms of the interplay between the fourfold and sixfold anisotropy parameters as a function of the composition. To validate their prediction the authors carried out three-dimensional phase-field simulations and plotted the results in an orientation selection map which is a space of ε_1 vs - ε_2 as shown in Fig. 1.3. The map consists of three different growth domains: a region of <100> dendrite growth, a <110> growth region and an intermediate regime called the hyperbranched dendrite growth region, where a continuous change of growth angle as measured from the <100> direction is observed. Haxhimali et al. have also experimentally examined this hypothesis of change in growth orientation by analysing the

dendrite growth in solidified Al-Zn alloys. Their experimental results showed that the growth directions changed smoothly from <100> to <110> with the addition of Zn.

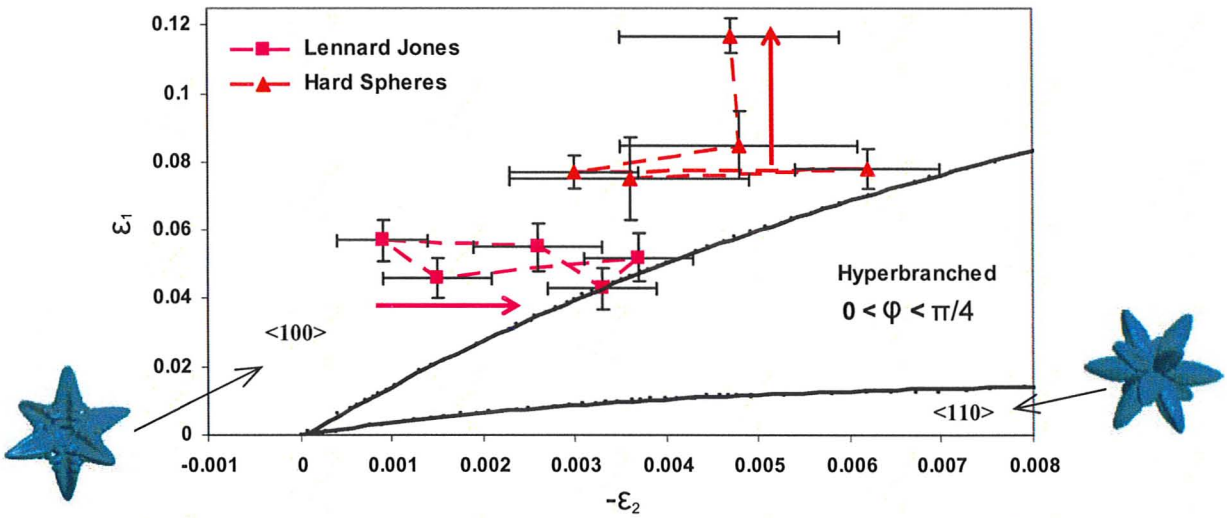

Fig. 1.3: Superimposing the anisotropy results of LJ and HS systems in Orientation Selection Map derived from phase field simulations[32]

The first confirmation of variations in crystal-melt γ anisotropies with solute additions was found by Becker et al.[31] where the changes in ε_1 and ε_2 were computed using CFM analysis for a binary Lennard-Jones (LJ) system with no atomic size mismatch and different bond strength between the elements. They have shown in the orientation selection map that variations in the magnitude of anisotropy are sufficiently large to induce changes in dendrite growth directions. This result of LJ system is summarized in Fig. 1.3 where the pink arrow shows the direction of variation in anisotropy parameters with solute addition indicating the corresponding change in dendrite growth selection. The LJ system showed a considerable amount of shift in ε_2

values. In contrast, Amini and Laird[32] studied the compositionally dependent anisotropy in γ for a binary hard sphere (HS) system with a diameter ratio of 0.9 and investigated the variation in ε_1 and ε_2. Their result is also superimposed in Fig. 1.3 for predicting the change in orientation of dendrite growth with composition. The result of the HS system exhibits a significant change in ε_1 , with little change in ε_2.

The Hard Sphere system, studied by Amini and Laird, varied from LJ system, studied by Becker, in terms of the variation in bond strength (i.e. energy mismatch) and size difference between the species. LJ system was characterized by energy mismatch but no size difference while HS system had only difference in atomic size with no mismatch in energy between the elements. The HS and LJ results of variation in anisotropies lead to the suggestion by Amini and Laird that atomic size mismatch affects primarily the ε_1 parameter whereas the anisotropy in energy controls the magnitude of ε_2. These speculations motivate the current study to carry on with the Al-Mg alloy system, which exhibits both a significant atomic size mismatch and variations in bond strengths to predict the possible changes in the dendrite growth directions as a function of composition.

1.5 Objective of the Project

The purpose of this research work is focused on the prediction of preferred orientation for the growth of dendrites in the Al-Mg system, that is, how do the crystal-melt interface properties and their associated anisotropy affect the selection of dendrite

growth orientation. The objectives of this project are: (1) to optimize the interatomic potential of Al-Mg system by comparing the Al-rich part of the Al-Mg equilibrium phase diagram and liquid enthalpy of the mixing with that of experiment. The potential is optimized to simulate the equilibrium crystal-melt interface and to compute the solid-liquid interface (SLI) properties , (2) to compute interfacial stiffness and interface free energy of binary Al-Mg alloys as a function of orientation and solute concentration using CFM technique. The analysis of the anisotropy parameters of interfacial energy will suggest the possible change in growth direction with solute addition, (3) to determine the kinetic coefficient of the interface growth of pure Al for different orientation that describes the crystallization dynamics.

The rest of the thesis is organized as follows. First, the simulation techniques and their employment to optimize the inter-atomic potential are described in chapter 2. Then chapter 3 describes the details of the anisotropic interfacial free energies computation and prediction of the dendritic growth direction of Al-Mg alloys utilizing the solute induced anisotropy parameters. Finally, the determination of interface mobility of (100) and (110) oriented interfaces from MD simulation methods is described along with some corrections which are applied to obtain accurate values. The last section will summarize the study and offer some suggestions for future work.

CHAPTER 2

Inter-atomic Potential Optimization

An inter-atomic potential is a formulation that describes the solvent-solvent, solvent-solute and solute-solute interactions during atomistic simulations. The Al-Mg potential, which is optimized in this study, was recently developed by Mendelev[40] and this potential is specially developed for the studies of solidification phenomena describing the solid-liquid phase equilibria and is mainly focused at dilute Mg solutions in Al. The full description of this potential can be found in Ref. [41] in tabular form. The optimization described in this chapter involves matching the equilibrium phase diagram, in particular the solidus and liquidus, of the model Al-Mg system to the experimental phase diagram. To determine the solidus and liquidus phase boundaries, Monte Carlo (MC) simulation is employed in association with a thermodynamic integration technique. This technique is first described by Ramalingham[42] and has been applied for several alloy system[42-44]. In this method, the free energy of both solid and liquid phases is calculated as a function of alloy concentration and then the solidus and liquidus compositions are derived from the common tangent construction. The first step of this procedure is to determine accurately the melting point (T_M) of the pure solvent species, which is aluminum (Al) in this study.

2.1 Melting Point Determination

The determination of melting point involves two steps. In the first step, Molecular Dynamics (MD) simulations are performed on systems containing both the solid and liquid phase in $NAP_{zz}T$ ensemble at various trial temperatures near the experimental T_M. In this ensemble, the total number of atoms and temperature are kept fixed and the dimension in the direction normal to the interface (along z) is allowed to change throughout the simulation in order to maintain zero pressure in that dimension (i.e. $P_{zz} = 0$) while the cross-sectional area A is held fixed. The growth velocity of the moving interface is observed by monitoring the total potential energy of the system over the course of simulation at each temperature. Then an approximate melting point is obtained by extrapolating the temperature to the point where the interface velocity is zero. Below the melting point crystal part of the cell will grow at the expense of liquid portion while above the melting point crystalline portion will melt and hence at T_M the growth would become stationary. This procedure will bracket the melting point with a fairly large uncertainty.

A second step is required to reduce the uncertainties on T_M, which will lead to the accurate determination of phase boundaries. For this purpose, a coexistence approach[45,46] is utilized where MD simulation is performed on the solid-liquid system in micro-canonical (NVE – fixed energy, volume and particle number) ensemble at the melting point estimated from the first step. The constant energy ensemble will equilibrate the co-

existing solid and liquid phases over the course of the simulation by adjusting the temperature. Multiple iterations of this NVE simulation are required to obtain a zero stress melting point while the solid and liquid part of the simulation cell will relax the pressure and maintain it nearly to zero. The melting point of pure Al derived from this potential is T_M = 926K which can be compared with the experimentally measured value of 933K.

2.2 Thermodynamic Integration Technique

The thermodynamic integration calculations begin by deriving the difference in free energy between solid and liquid phases as a function of temperature for pure solvent (Al). These quantities serve as a reference points for the integration of the Gibbs free energy as a function of solute composition at each temperature. The thermodynamic relation between free energy and enthalpy per atom follows:

$$\left(\frac{\partial(G/T)}{\partial T}\right)_P = -\frac{H}{T^2} \tag{2.1}$$

In MD simulations, the enthalpy of an equilibrated system is equivalent to the total energy of that system at zero pressure. The Eq. 2.1 can be integrated from the melting point to calculate the solid-liquid free energy difference according to the following expression:

$$\frac{G^S - G^L}{T} = \int_T^{T_M} \frac{H^S(T') - H^L(T')}{T'^2} dT' \tag{2.2}$$

G is the free energy of pure solid (S) or liquid (L) phases for the solvent species while H denotes the enthalpy. The temperature dependent enthalpy values are computed for a series of seven temperatures in the vicinity of melting point and the expressions for the right hand side of Eq. 2.2 are obtained from a least square fit of these data to a straight line. The results are shown in Fig. 2.1 where the top curve refers to the liquid phase and the bottom one represents the solid phase. The latent heat of pure aluminum is found to be 0.1118 eV/atom.

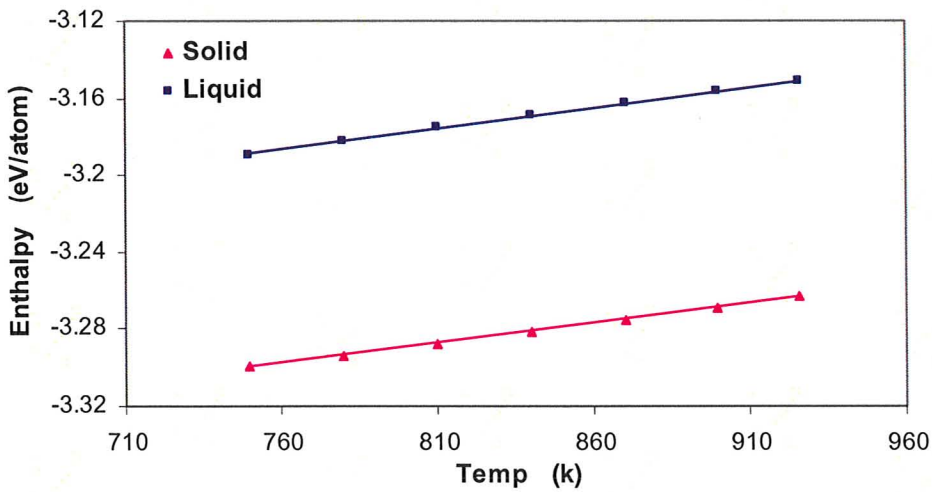

Fig. 2.1: Enthalpy for the solid and liquid phases of pure Al as a function of temperature

2.3 Employment of Monte Carlo Simulation

In the thermodynamic integration technique, phase boundary determination is coupled with the calculation of free energy vs. solute composition, which is obtained through the employment of Monte Carlo (MC) simulations in the so-called semi Grand Canonical ensemble[47,48]. SGCE refers to the system of fixed chemical potential

difference between solute and solvent species, $\Delta\mu = \mu_{Mg} - \mu_{Al}$, fixed temperature and total number of atoms with variable number of Al and Mg atoms, that is, the solvent and solute atoms can switch types. Actually MC simulation allows the system to change relative composition depending on the applied external driving force ($\Delta\mu$ and T) during the simulation. In these simulations, an external chemical potential is imposed which leads the system to a stable state by adjusting the solute concentration over the course of simulation and eventually an equilibrium composition is achieved corresponding to that applied $\Delta\mu$ for each specific temperature.

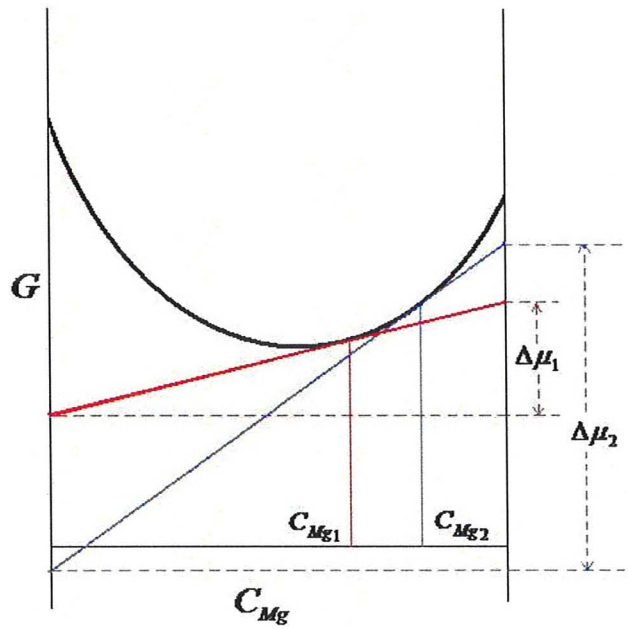

Fig. 2.2: Principle of Monte Carlo simulation showing the change in solute concentration with the variation in chemical potential differences between the species

The principle of the Monte Carlo simulation is illustrated schematically in Fig. 2.2. This is a schematic plot of free energy as a function of the solute composition, which

is Mg in this study. The difference between end points, that intersect the G axes, of a tangent drawn to the free energy curve represents the chemical potential difference while the point at which it is tangent to the curve describes the equilibrium composition for that $\Delta\mu$. If $\Delta\mu_1$ is applied to the system, this will produce C_{Mg1} while imposing a higher value $\Delta\mu_2$ will results in a higher magnitude of solute concentration C_{Mg2}. Through this procedure the whole range of Mg composition is calculated by varying the chemical potential difference starting from some low value in the MC simulation. Fig. 2.3 shows some snapshots of equilibrated systems that are taken from the simulation of the liquid phase at a temperature of 900K: the silver color atom represents Al while the golden color atom represents Mg. The corresponding compositions are mentioned in each snapshot where the 10, 20 and 40% Mg resulted from an imposed chemical potential difference of 1.775, 1.85, 1.925 eV/atom respectively.

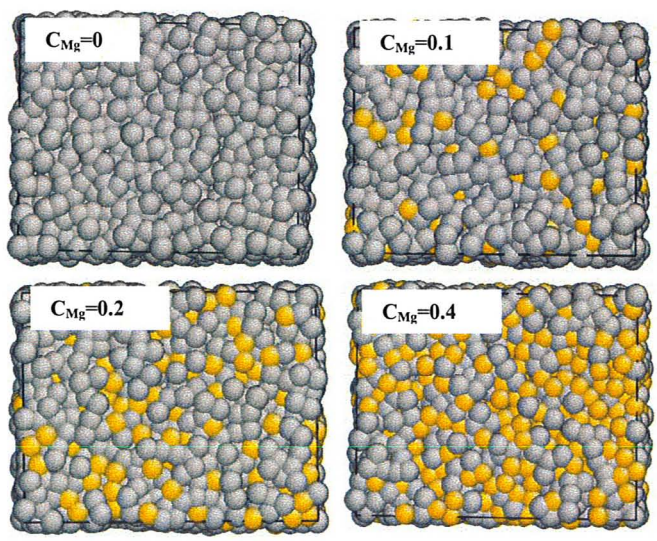

Fig. 2.3: Snap shots from MC simulation of Al-Mg alloys with different composition. The 10, 20 and 40% Mg correspond to $\Delta\mu$ of 1.775, 1.85, 1.925 eV/atom respectively

In the present work Monte Carlo simulation cells of 4×4×4 unit cells and 2048 atoms are employed. Two sets of simulations are performed for each chemical potential difference. The first run of $1x10^5$ steps per atom was used to equilibrate the system and the second one with the same run time was used to generate sufficient statistics for the composition. A series of six temperatures are investigated to determine the phase boundaries and roughly sixteen chemical potential differences were investigated at each temperature in order to span the entire range of Mg compositions.

2.4 Free Energy Calculation

The final step in the phase boundary determination is the free energy calculation. The free energy for both solid and liquid phases is calculated as a function of solute concentration from the knowledge of chemical potential difference vs composition derived from MC simulation. For this purpose, another integration approach is applied which utilizes the following thermodynamic relation:

$$\left(\frac{\partial G}{\partial C_{Mg}}\right)_{P,T} = \Delta\mu\left(C_{Mg}, T\right) \tag{2.3}$$

where G is the Gibbs free energy per atom. Actually Eq. 2.3 is the definition of chemical potential of a binary system at constant pressure and temperature. As discussed by Ramalingham *et al.* [42], for the purpose of integrating the above relationship in Eq. 2.3, MC results of imposed $\Delta\mu$ and the corresponding ensemble average of the composition C_{Mg} can be fitted to the following functional form:

$$\Delta\mu\left(C_{Mg},T\right)=k_B\,T\ln\left(\frac{C_{Mg}}{1-C_{Mg}}\right)+\sum_{i=0}^{n}A_i C_{Mg}^{i} \tag{2.4}$$

where k_B is Boltzmann's constant. The first term on the right hand side of the above equation corresponds to the ideal contribution to the chemical potential difference while the second term represents a non-ideal effect. The non-ideal contribution is measured from a polynomial fit in concentration with coefficients A_i and for the optimization of this Al-Mg potential a fourth order polynomial fit is utilized. To calculate the free energy of both solid and liquid phases, Eq. 2.4 can be integrated giving the following functional expression of G vs. concentration for each phase:

$$G(T,C_{Mg})=G(T,C_{Mg}=0)+k_BT[C_{Mg}\ln C_{Mg}+(1-C_{Mg})\ln(1-C_{Mg})]+\sum_{i=0}^{n}\frac{A_iC_{Mg}^{i+1}}{i+1} \tag{2.5}$$

where the first term on the right hand side is the free energy of pure Al, the second term represents ideal part of free energy and the third one comes from the excess contributions to G. For the calculation of free energy across the entire composition range, free energy of pure Al for the solid phase is considered as the reference state and G_{Al}^{S} is taken as zero while the free energy of liquid Al, G_{Al}^{L}, is given by the measured value of $G_{Al}^{S}-G_{Al}^{L}$.

2.5 Phase Boundary Determination

The equilibrium solidus and liquidus phase boundary compositions are determined from the knowledge of computed Gibbs free energy vs. composition behaviour of each phase. There are two ways to determine the phase boundaries: first is

the simple "common tangent construction" applied to the solid and liquid free energy curves, that is, a line tangent to G vs. C_{Mg} of both phases. The points where this tangent line intersects the free energy curves of solid and liquid phases will determine the solidus and liquidus composition of the coexisting phases respectively which are in equilibrium at that specific temperature.

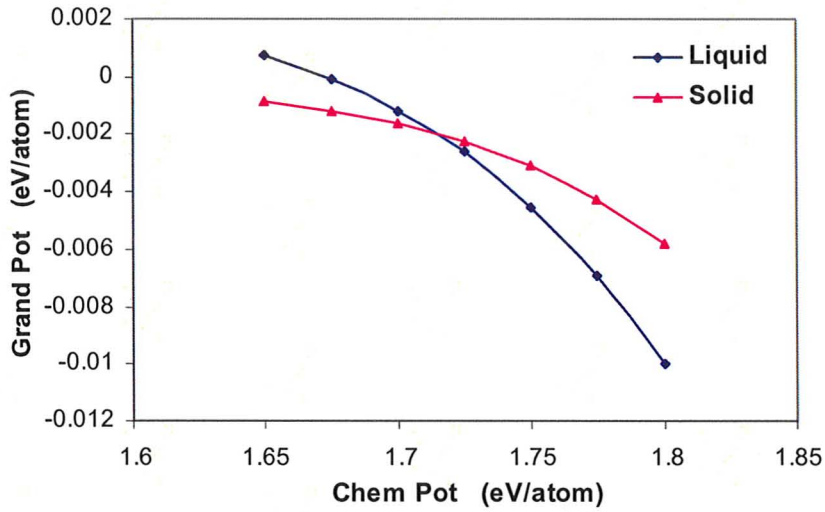

Fig. 2.4: Grand potential functions for solid and liquid phases at 900K

The second method is the computation of phase boundaries from the grand potential function. Actually the grand potential is the thermodynamic potential of an isothermal system where the chemical potential of the system is kept constant. The thermodynamic formulation of this potential is as follows:

$$\Omega = G - \Delta\mu C_{Mg} \qquad (2.6)$$

where Ω represents the grand potential function. In this study, the solidus and liquidus compositions are determined utilizing this method. Fig. 2.4 describes a sample plot of Ω vs. $\Delta\mu$ for the both solid and liquid phases at the temperature of 900 K. This plot shows

that the grand potential functions intersect each other at some point, which represents the chemical potential in equilibrium at that particular temperature. The equilibrium phase boundaries can be obtained for that temperature by imposing this chemical potential to the system in MC simulation.

2.6 Fitting Potential to Phase Diagram

In the procedure of potential optimization, several potentials have been tried to reproduce the Al-rich side of the real Al-Mg phase diagram. The failure of couple of earlier potentials to determine the phase boundaries properly limits their application in simulation studies of solidification in this alloy. The phase diagram determined from potential #A (corresponding to potential #2 in Ref. [40]) is shown in Fig. 2.5 which illustrates that this potential overestimates the phase boundaries in comparison to that of experimental results. Then to improve the accuracy of solidus and liquidus compositions, the following technique is used for fitting the potential to the phase diagram.

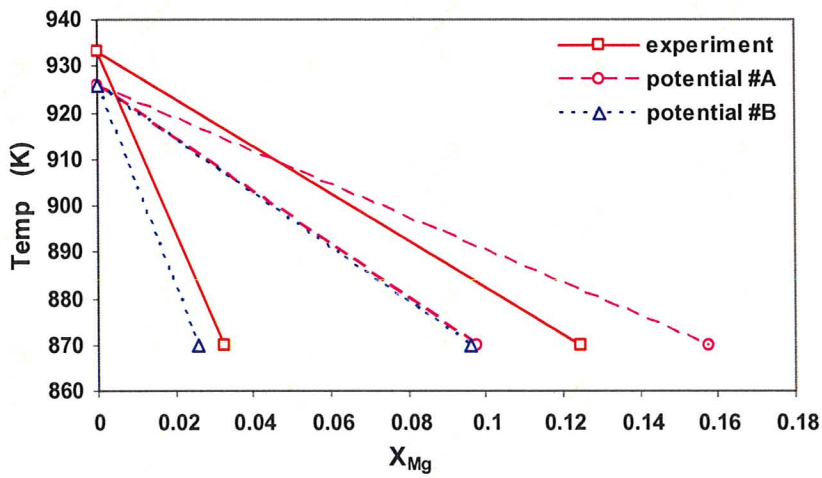

Fig. 2.5: Al-Mg phase diagram determined from potential #A and #B

As potential #A overestimates the phase boundaries, our aim was to decrease the Mg concentrations of equilibrium solidus and liquidus compositions for the improvement of the potential. Potential #A was determined by fitting to, among other parameters, the experimental enthalpy of mixing of the liquid (taken from the Ref. [49]) as a function of composition. Therefore, the modification in the potential can be done by decreasing the target value of the liquid enthalpy of mixing only without changing that of solid phase. For this purpose, one term, given by $\beta C_{Mg}(1-C_{Mg})$, is subtracted from the liquid enthalpy of mixing, where β is a parameter which is tuned to obtain a better agreement with the real Al-Mg phase diagram. This approach is illustrated in Fig. 2.6 where the free energy is plotted as function of composition calculated at the temperature of 870K.

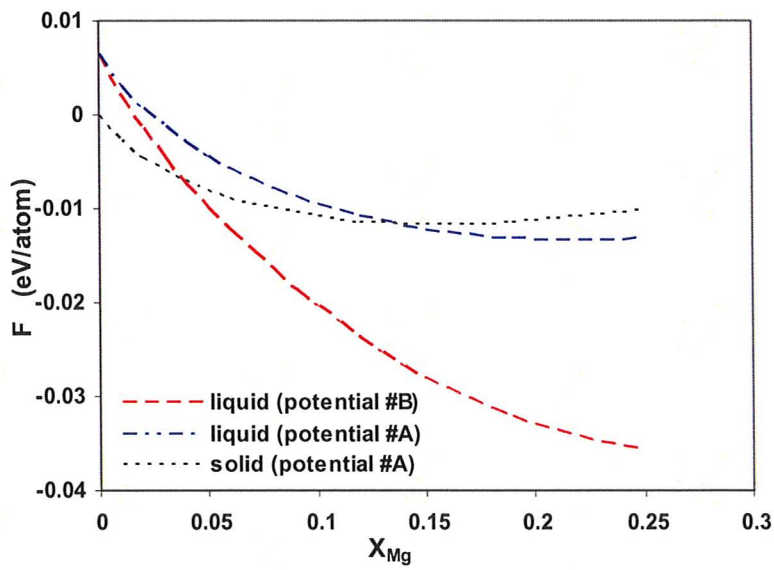

Fig. 2.6: Free energy of the liquid and solid phases calculated with potential #A and #B at T=870 K showing the fitting technique

As the target value of the liquid enthalpy of mixing is decreased the free energy curve is shifted downward as shown by the change from the blue curve to red curve. The amount of decrease in the free energy curve can be controlled by the choice of the value of β. This method leads to a new potential (#B) (corresponds to potential #3 in Ref. [40]) and the construction of common tangents between the free energy curves of the solid and new liquid phase considerably decreases the Mg concentrations in the both solidus and liquidus compositions. Hence potential #B better reproduces the real Al-Mg phase diagram compared to that of potential #A which is shown in Fig. 2.5. Actually the new potential underestimates the phase boundaries.

So, we have obtained two potentials: one (#A) overshoots the phase boundaries while the other (#B) undershoots those. Based on these data, a new potential (#C) (corresponds to potential #4 in Ref. [40]) is determined with a linear combination of the liquid enthalpy of mixing of earlier two potential #A and #B to obtain better agreement with the phase diagram. Eventually this potential almost reproduces the solidus and liquidus compositions which lie very close that of the real Al-Mg phase diagram, the final result is shown in Fig. 2.7.

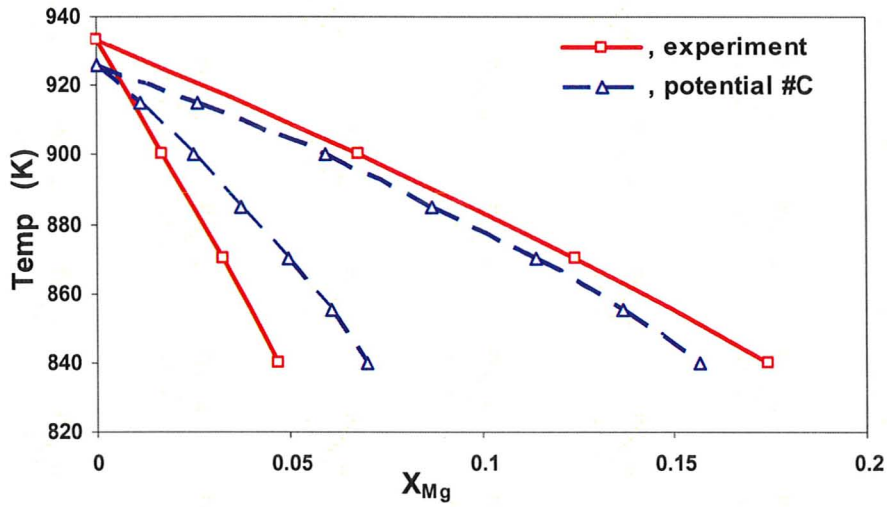

Fig. 2.7: Al-Mg phase diagram showing comparison between the results obtained from this potential and from experiment

2.7 Al-Mg Phase Diagram

The Al-rich side of the best fitted temperature-composition Al-Mg phase diagram determined from the inter-atomic potential is shown in Fig. 2.7. The phase boundaries with solid red lines represent the experimental results while blue dotted lines reflect the results of this potential. The Al-rich side of the phase diagram is well reproduced by this potential. The equilibrium data of some parameters for the coexisting-phases of this phase diagram are summarized in Table 2.1. This table lists the solidus and liquidus compositions (x^s_{Mg} and x^l_{Mg}) and lattice parameters (L^s, in °A) of the solid phase. It also includes the equilibrium chemical potential difference ($\Delta\mu$, in eV/atom) between the species along with the total atomic densities (ρ^s_{tot} and ρ^l_{tot}) for both phases. The data are

generated from sufficient statistics of stress free equilibrated phases utilizing Monte Carlo (MC) simulations.

TABLE 2.1: Solidus and liquidus compositions, equilibrium chemical potential differences, lattice parameters and total atomic densities for each of the temperatures

T (K)	$\Delta\mu$ (eV/atom)	x^s_{Mg}	x^l_{Mg}	ρ^s_{tot} (A^{-3})	ρ^l_{tot} (A^{-3})	L^s (A)
840	1.8095	0.0703	0.1565	0.0560	0.0528	4.1483
855	1.7951	0.0608	0.1363	0.0560	0.0529	4.1474
870	1.7758	0.0496	0.1139	0.0561	0.0531	4.1455
885	1.7499	0.0372	0.0871	0.0562	0.0532	4.1436
900	1.7144	0.0251	0.0594	0.0563	0.0533	4.1424
915	1.6461	0.0112	0.0263	0.0564	0.0534	4.1403

2.8 Liquid Enthalpy of Mixing

Enthalpy of mixing is defined as the change in the enthalpy due to the change in the system from pure components to the mixture of different solute concentration. When two substances are mixed at constant temperature, heat may be given off from the system (total enthalpy is less than before mixing) or absorbed by system (enthalpy after mixing is greater). The total enthalpy of mixture is therefore different from that calculated from the mixture ($H = H_A C_A + H_B C_B$) of the enthalpies of pure substances at the same temperature. The excess amount of enthalpy is known as the enthalpy of mixing. The concept of enthalpy of mixing is shown in Fig. 2.8 where the dotted straight line represents the mixture.

The enthalpy of mixing, ΔH_M, is determined by subtracting the composition weighted enthalpy of pure Al and pure Mg. The expression of ΔH_M is as follows:

$$\Delta H_M = H - H_{Al}(1 - C_{Mg}) - H_{Mg}C_{Mg} \tag{2.7}$$

where H is the enthalpy per atom of the solution of Al-Mg system with a Mg mole fraction of C_{Mg}, H_{Al} and H_{Mg} are enthalpy of pure Al and Mg respectively.

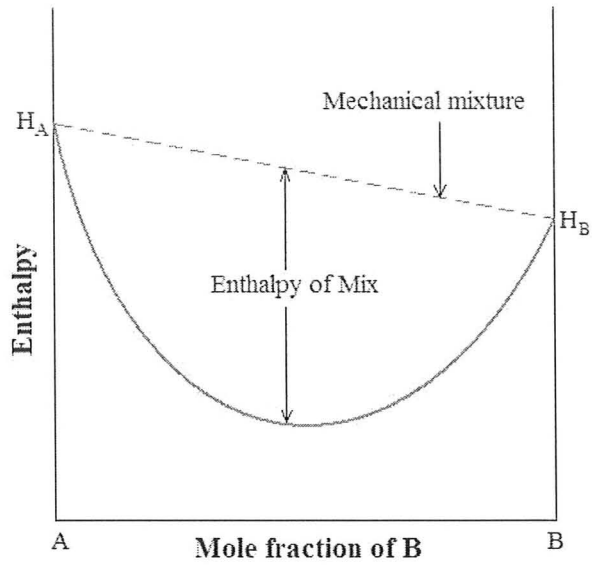

Fig. 2.8: The concept of enthalpy of mixing

We have optimized this potential by comparing the optimized liquid enthalpy of mixing obtained from this potential with the experimental results. The results of enthalpy of mixing for the liquid phase as a function of Mg concentration are shown in Fig. 2.9 where a negative ΔH_M contribution is observed at the dilute Mg solutions in Al of the Al-Mg system. The liquid enthalpy of mixing obtained by this potential is comparable with other experimental results, but it is somewhat lower than that derived through a recent CALPHAD assessment of the Al-Mg phase diagram[49]. However, there is considerable scatter in the experimental enthalpy of mixing data, and in comparison to that the prediction of this potential is not unreasonable.

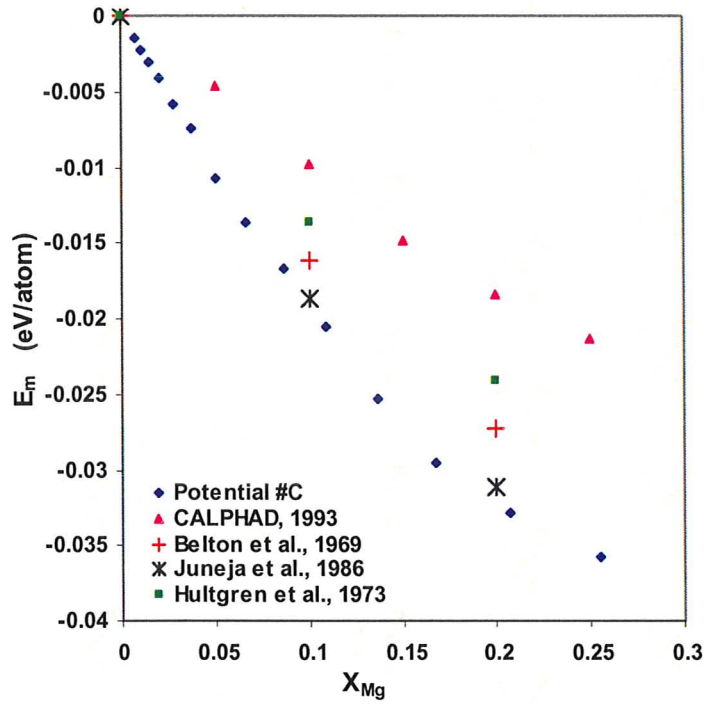

Fig. 2.9: Enthalpy of mixing of liquid Al-Mg alloys at T=900 K obtained from MC simulation with this inter-atomic potential and from [49], [50], [51], [52].

2.9 The Miscibility Gap

Generally the experimentally determined phase diagram[49,53-56] shows no miscibility gap in the temperature–composition phase diagram of Al-Mg system in either the solid or liquid phase. In contrast, the presence of a miscibility gap is one of the distinctive characteristics of this Al-Mg inter-atomic potential. Actually miscibility gap refers to a region of metastability in which one phase system will decompose into two equilibrium phases of essentially same structure with no solubility in one another. We have conducted some investigations to examine the indications of the miscibility gap in

this potential. Basically this phenomenon is observed to start below a critical temperature, T_c. The chemical potential difference between the species at $T<T_c$ would be same for all compositions inside the entire region of miscibility gap. In Monte Carlo simulation, the response of imposing this constant value of $\Delta\mu$ would result in a discontinuous jump in terms of the equilibrium solute concentration. These discrete changes in the solute concentration observed in this potential are illustrated in Fig. 2.10 showing a hysteresis in the chemical potential curve vs Mg composition which indicates the existence of miscibility gap.

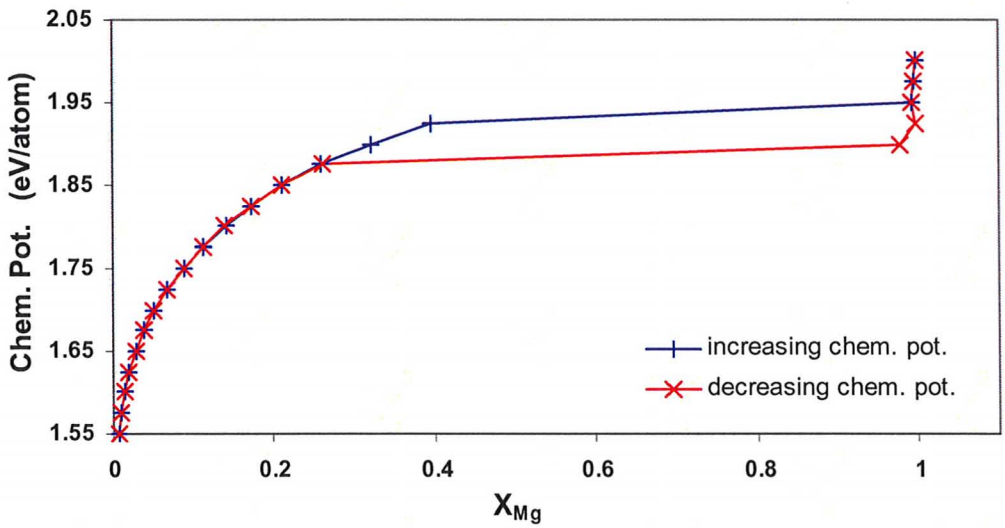

Fig. 2.10: Chemical potential difference vs solute concentration showing hysteresis as a signal of the presence of miscibility gap at 870 K in liquid phase

During the scanning of $\Delta\mu$ in MC, if the simulation starts with lower chemical potential difference and $\Delta\mu$ is increased, the trend shown by the blue line with the '+' symbols in Fig. 2.10 will result. In the reverse sense, that is by decreasing $\Delta\mu$ starting

from higher values the system tracks the red line represented by the '×' symbols. The hysteresis observed has taken place because when $\Delta\mu$ is increased (decreased) the system is trapped in a metastable state as it enters into the miscibility gap region and then further increase (decrease) in $\Delta\mu$ lead the system to switch over to a stable state showing a discontinuous jump in concentration in Fig. 2.10.

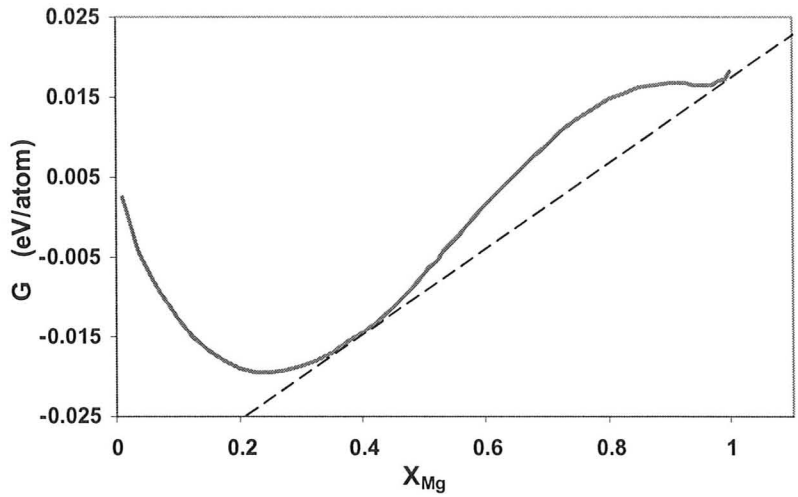

Fig. 2.11: Free energy curve for the liquid phase showing two peaks which corresponds to two equilibrium phases as an indication of miscibility gap at 870 K in liquid phase

An alternative means of identifying the presence of a miscibility gap is the free energy vs composition curves. This is also investigated in this study and is illustrated in Fig. 2.11 where the free energy curve shows two minima, which is an indication of the existence of two equilibrium phases in that region. The common tangent construction will give the composition of the miscibility gap boundaries corresponding to those equilibrium

phases. The free energy vs. composition proves the presence of miscibility gap at higher Mg concentration.

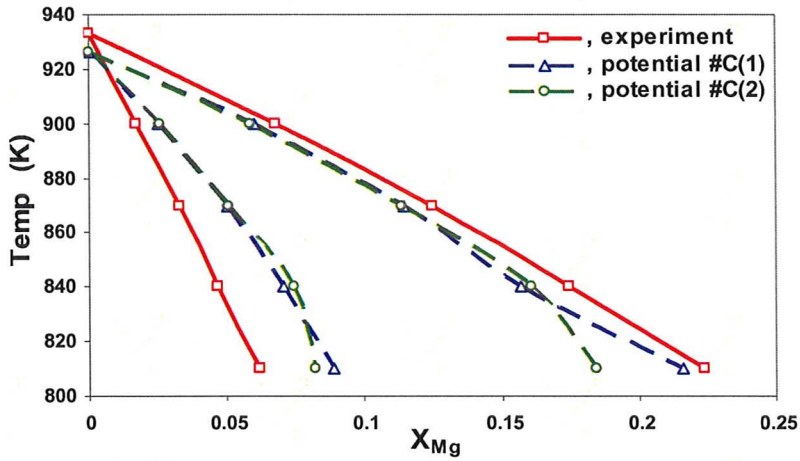

Fig. 2.12: Al-Mg phase diagram showing the deviation of the phase boundaries due to the presence of miscibility gap

It is investigated that this potential produces good results in terms of the phase boundaries up to around 16% Mg in liquid phase which corresponds to 840K. Below the temperature of 840K, the equilibrium chemical potential difference $\Delta\mu$ enters into the region of miscibility gap. The phase boundaries determined from MC at 810K lead to some deviations in the solidus and liquidus line from their natural trend. This is illustrated in Fig. 2.12. The different dotted lines, represented by potential #C(1) and #C(2), are obtained from the potential #C with different polynomial fit of the free energy curves. The blue dotted line, labelled with potential #C(1), is obtained by fitting the data of the dilute Mg side only while the green dotted line, labelled with potential #C(2), is obtained by fitting the data of the entire Mg range. It is observed that the miscibility gap in this

potential has affected the phase boundaries at the temperature lower than 840K. Below this temperature, the boundaries of the miscibility gap at the Mg poor side (~ 16% Mg) extend all the way to the Mg rich side of the phase diagram. Even for the Mg-1%Al alloys the potential is found to be in the region of miscibility gap which leads us conclude that this interatomic potential of Al-Mg system is not appropriate for the simulation of Mg-rich alloys. This potential is accurate from the melting point of pure Al (926K) to the temperature of 840K and correspondingly from pure Al to around Al-7%Mg for the solid phase and up to around Al-16%Mg for the liquid phase.

CHAPTER 3

Computation of Interfacial Stiffness, Interfacial Free Energy and its Anisotropy

The formation of dendrites during solidification is a very important process from the perspective of both academic research and industrial technology as the complex morphology of dendrites critically controls the material properties of the cast alloys. Numerous studies over the past two decades have demonstrated the crystal-melt interfacial free energy (γ), defined as the work required to create a unit area of interface between the crystal and its own melt, and its orientation $(\hat{n})$ dependence as one of the crucial factors in determining the dendritic evolution[57]. Specifically, the dendritic growth directions and their kinetics are known to be extremely sensitive to the weak anisotropy of γ in metallic systems[58].

In atomic scale simulation, for the accurate measurement of the orientation dependence of γ another solid-liquid interface property known as the interfacial stiffness is computed. Stiffness is defined as $\gamma + \gamma''$ while $\gamma'' = d^2\gamma/d\theta^2$ and θ is the angle between the growth direction and the direction normal to the interface. Actually this quantity is an order of magnitude more anisotropic than γ itself. For a crystal with cubic

symmetry, the weakly anisotropic interfacial energy is traditionally approximated[4,6,8-9] by $\gamma(\theta) = \gamma_0(1 + \varepsilon \cos 4\theta)$ where ε is anisotropy parameter. Then the interfacial stiffness is given by $\gamma + \gamma'' = \gamma_0(1 - \beta \cos 4\theta)$ with $\beta = 15\varepsilon$ which is showing that stiffness is 15 times more anisotropic than the interfacial energy. Basically stiffness can vary significantly as a function of orientation and hence largely control the orientation dependence of the fluctuations of solid-liquid interface during atomistic simulations. That is why, generally, the stiffness anisotropy is more feasible to compute from Molecular Dynamics simulations than that of γ and the latter can always be calculated from the stiffness which will be discussed in section 3.6.

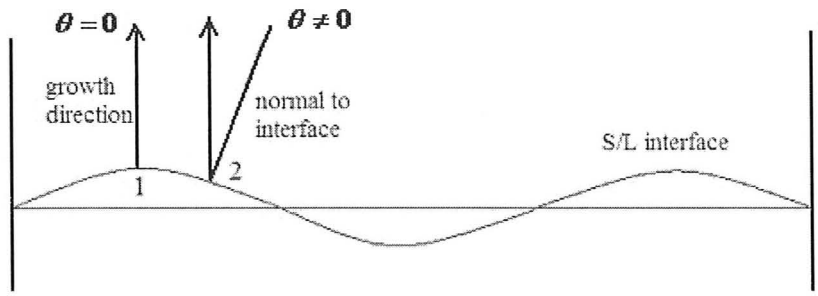

Fig. 3.1: Schematic plot of the curvature driven fluctuating crystal-melt interface

Actually, in the curvature driven interface fluctuation, stiffness is the key property that takes into account the effect of curvature in the computation of γ. This is illustrated in Fig. 3.1 where the wave represents the fluctuating solid liquid interface. At point 1 there is no dependence of θ, but in case of point 2, there is an angular difference between growth direction and normal to the interface. Stiffness considers this effect of curvature.

3.1 Difficulties in Experimental Measurement of γ

Experimentally, interfacial energy is estimated in two ways: one is indirect measurement and the other one is direct measurement. In the indirect measurement analysis, γ is estimated from the nucleation kinetics utilizing the classical nucleation technique[59-61]. This method shows an underestimation of the interfacial energy by 10-20%[32]. In this technique, the liquid is filtered to remove the heterogeneous nucleation sites which in turn affects the homogeneous nucleation rate and the determination of γ. Estimations of γ from nucleation techniques could not solve the problem of orientation dependence as the calculated values are orientationally averaged. The interpretation of the surface energy on impure systems was found to be very difficult in the nucleation method as γ can vary in a complex manner with temperature[62].

The direct measurement method involves the uses the geometry of the grain boundary groove at the solid-liquid interface. Actually this technique is based on the measurement of equilibrium contact angle between the grains at crystal-melt interface for the determination of anisotropy in γ. Due to the inherent difficulties associated with performing these experimental measurements, only a few handful materials[63,64] exist. Recently Napolitano[65-67] et al. developed a quantitative approach for the measurement of equilibrium crystal shape with low anisotropy of the interfacial energy through the use of a Wulff construction[60,68]. Then the fourfold anisotropy parameter of γ (only the anisotropy but not the magnitude of γ) was determined from that measurement of the

crystal shape. This procedure is applied for Al-Si, Al-Cu and Al-Sn binary alloys. The lack of accuracy in experimental measurements has paved the way for the development of atomic scale simulation techniques to map out the interfacial free energy and its anisotropic behaviour.

3.2 MD Techniques for Computing Interfacial Energy

Two complementary techniques have emerged for computing the interfacial free energy, γ and its anisotropy from MD simulations. One is the cleaving technique, first proposed by Broughton and Gilmer[69] and subsequently extended by Davidchack and Laird[70-72]. In this method, the computation of interfacial energy involves the calculation of the total reversible work to form the solid-liquid interface from two separate bulk solid and liquid phases. The orientation dependence of γ can be mapped out by repeating the procedure for various crystal orientations. The second technique is the capillary fluctuation method (CFM) pioneered by Hoyt et al.[20]. The CFM is based on the measurement of equilibrium height fluctuations in the solid-liquid interface to extract the interfacial stiffness. The cleaving technique possesses a distinct advantage of requiring around 10^4 atoms for its application. While the CFM involves typically 5-10 times more atoms than that of cleaving technique for the analysis. The extended cleaving method generally provides a more precise value for γ itself than that of CFM, but the measurement of anisotropy parameters results in larger uncertainties. In contrast, the CFM analysis is considered as the comprehensive technique for computing the anisotropy

of γ with higher statistical precision. The cleaving method has been used to calculate the γ for a variety of model system including hard spheres[70,73], soft spheres[72] and Lennard-Jones particles[69,71]. On the other hand, CFM has been extensively applied to the study in crystal-melt interface free energies in various elemental fcc and bcc metals[19-21,23,30], alloy system[22] and Lennard-Jones system[31,74-75] as well.

Actually, CFM is applied to compute the values of interfacial stiffness for several orientations and the results are then combined with an analytical expansion of $\gamma(\hat{n})$ to obtain the magnitude of γ and its associated anisotropy. For mapping out the full parameterization of orientation dependent interfacial free energy, a symmetry dependent cubic harmonic (linear combination of spherical harmonics that obey the cubic symmetry of the crystal) expansion of $\gamma(\hat{n})$ is employed in terms of Cartesian components of the interface normal $\hat{n}(=n_1, n_2, n_3)$ which is[76]:

$$\frac{\gamma(\hat{n})}{\gamma_0} = 1 + \varepsilon_1\left(\sum_{i=1}^{3} n_i^4 - \frac{3}{5}\right) + \varepsilon_2\left(3\sum_{i=1}^{3} n_i^4 + 66 n_1^2 n_2^2 n_3^2 - \frac{17}{7}\right) \qquad (3.1)$$

where γ_0 is the orientation averaged interface energy and ε_1 and ε_2 describe the measure of four and six fold anisotropy parameter respectively. The studies of CFM analysis in several elemental systems have described that both ε_1 and ε_2 anisotropy parameters are required to capture accurately the entire orientation dependence of interfacial energy and in turn for the dendrite growth directions. In this research work, CFM technique is employed to study the interfacial properties and their orientation dependence.

3.3 The Analysis of Capillary Fluctuation Method

In CFM, analysis starts with capturing the snapshots of crystal-melt systems which are equilibrated over the long MD run. These snapshots are utilized for determining the location of interface positions applying the order parameter measurement as described in Ref. [20]. In this technique, each atom is assigned with an order corresponding to its position in the solid or liquid phase. This measurement will be discussed in detail in section 3.6. The resulting fluctuated interface height profiles were then Fourier transformed to produce the instantaneous values of the fluctuation amplitudes $A(k,t)$ which are averaged over the all simulated configurations to yield $\left\langle |A(k_x,k_z)|^2 \right\rangle$. The CFM technique employs an analysis of this ensemble average interfacial amplitude to extract the interface stiffness (S) according to Eq. 3.2. The fluctuation spectra of a two-dimensional interface geometry will follow the following relation for sufficiently large wavelength[75]:

$$\left\langle |A(k_x,k_z)|^2 \right\rangle = \frac{k_B T}{a(S_{xx}k_x^2 + S_{zz}k_z^2 + 2S_{xz}k_x k_z)} \tag{3.2}$$

where $A(k_x,k_z)$ is the Fourier transform of the height of the fluctuating interface while k_x and k_z are the wave-vectors in two perpendicular directions parallel to interface and S_{xx} and S_{zz} are two corresponding stiffnesses which are illustrated below, a denotes the cross sectional area of the interface.

The crystalline symmetry can be used to simplify the form of Eq. 3.2 for computing interface stiffness for different orientations. The (100) oriented interface consists of a 4-fold and mirror-plane symmetry, which confirms that $S_{xx} = S_{zz} = S$ and $S_{xz} = 0$. This leads to the reduced form of Eq. 3.1 as:

$$\left\langle | A(k) |^2 \right\rangle = \frac{k_B T}{a S k^2} \tag{3.3}$$

For the (110) oriented interface, due to the presence of 2-fold symmetry and mirror-plane, the diagonal contribution to the stiffness is not equal i.e. $S_{xx} \neq S_{zz}$ and $S_{xz} = 0$. Then the Eq. 3.2 will take the form:

$$\left\langle | A(k_x, k_z) |^2 \right\rangle = \frac{k_B T}{a(S_{xx} k_x^2 + S_{zz} k_z^2)} \tag{3.4}$$

The interfacial free energy (γ) and its anisotropy are then computed from the analytical expansion of $\gamma(\hat{n})$ as described in Eq. 3.1 utilizing these stiffness values.

The CFM approach described here has been illustrated in the past for thin slab like simulation cell[20-22] containing quasi-one-dimensional (quasi-1D) fluctuating interface which is extended[77] later on for two-dimensional (2-D) solid-liquid interface. In this present study 2-D interface geometry is employed because of its advantages over quasi-1D interface. Crystal-melt interfaces with 2-D geometry requires only two simulations with (100) and (110) interface normals to compute three independent stiffness values from which interfacial free energy and its associated anisotropy can be derived,

while quasi-1D interface is required with three independent simulations for calculating the magnitude and anisotropy of interfacial energy.

3.4 Simulation Procedure for Binary Al-Mg alloy

Application of the CFM analysis requires well-equilibrated solid-liquid systems with a fluctuating interface. A combination of Molecular Dynamics (MD) and Monte Carlo (MC) simulation, as described in Ref. [44], is utilized for the equilibration of all systems. The MC simulations are employed to allow the composition change for obtaining a solid liquid system with the equilibrium solidus and liquidus composition at each temperature. MC equilibrates the system in terms of the composition profile. The MD simulations are applied to relax the pressure of the simulation cell and to collect the statistics of the fluctuating crystal-melt interfaces. For binary Al-Mg alloys, six simulation cells were set up at six different temperatures according to the equilibrium lattice parameter, phase-boundary compositions and bulk densities of solid and liquid phases at each specific temperature whose values are determined from the phase diagram calculations (Table 2.1). And in all cases, we have considered simulation cells with both (100) and (110) oriented crystal melt interfaces. For the (100) oriented interface, the solid-liquid systems were created with 64000 atoms ($20 \times 40 \times 20$ fcc unit cells) while for the (110) oriented interface, the system contains 62720 atoms ($20 \times 28\sqrt{2} \times 14\sqrt{2}$ fcc unit cells).

The equilibration procedure was initiated by generating the simulation cell of pure solvent (Al) with the fcc crystal structure at all temperatures. The system is loaded with the equilibrium number of solute atoms for the solid phase at both ends and for the liquid phase at the interior region at each corresponding temperature. The middle ½ of the simulation cell is then melted along y direction using Monte Carlo simulation creating periodic solid-liquid boundaries. After the melting step, the solid-liquid system was moved to MD simulation with $NAP_{yy}T$ ensemble for relaxing the pressure generated in the system. In MD run the simulation cell was under no constraint condition in the direction normal to the interface, i.e. $P_{yy} = 0$, as it was allowed to change length in that direction to compensate the volume changes during the simulation while the interfacial area, a, was kept fixed to ensure a strain-free crystal. The average temperature is maintained using a Nosé-Hoover thermostat. The MD run was carried out up to 10^6 time steps and the system was then returned to MC to equilibrate it with runs of approximately 3×10^3 steps per atom employing a chemical potential difference between the species at which both solid and liquid phases are in equilibrium for a given temperature. The same run time was used again for the final relaxation of composition profiles. Semi Grand Canonical ensemble (SGCE), as described in Section 2.3, was applied in MC to facilitate the composition change in the system.

To generate sufficient statistics for the fluctuation spectrum $\left\langle |A(k_x,k_z)|^2 \right\rangle$ of the solid-liquid interface, MD runs were performed on the system in a micro-canonical (NVE) ensemble for 6×10^6 time steps, in the time length of 6 ns. The snapshots are

collected after every 500 time steps producing a total of 12000 configurations for each alloy composition. These captured snapshots are then used for studying the solid-liquid interface and their properties in CFM analysis. All the MD simulations of this study used the LAMMPS (Large-scale Atomic/Molecular Massively Parallel Simulator) code[78,79].

3.5 Interfacial Stiffness Extraction

The long MD runs produced a collection of 12000 snapshots of equilibrated solid-liquid systems. To extract the values of interfacial stiffness, the capillary fluctuation method requires identification of the interface location for each snapshot. Actually the position of the crystal-melt interface is located employing the order parameter measurement technique[20], by means of labelling an atom as being in either the solid or liquid phase in the simulation, which utilizes the following expression:

$$\phi = \frac{1}{12}\sum_i \left|\vec{r}_i - \vec{r}_{fcc}\right|^2 \qquad (3.5)$$

where $\vec{r}_{fcc}$ corresponds to ideal fcc position in the crystal, $\vec{r}_i$ denotes the instantaneous atom position, i refers to the nearest neighbour positions of an fcc atom over which the summation is taken and 12 represents the total number of nearest neighbour atoms. Basically, the local structural order parameter measures deviations of the nearest neighbours of a given atom from their ideal fcc positions and then considers the sum of the all deviations. A typical profile of the order parameter is shown in Fig. 3.2 for a single configuration of the solid-liquid system of (110) oriented interface at the temperature of 915K. In Fig. 3.2, the order parameter is an average quantity over all the atoms at each

corresponding y-position. As ϕ enters into the liquid region, a large deviation from the ideal position is observed which is associated with a jump in the order parameter profile. The value of ϕ at the interface is roughly half way between the average order parameter values of bulk solid and that of liquid phase. It was found that $\phi \approx 0.95$ at the interface.

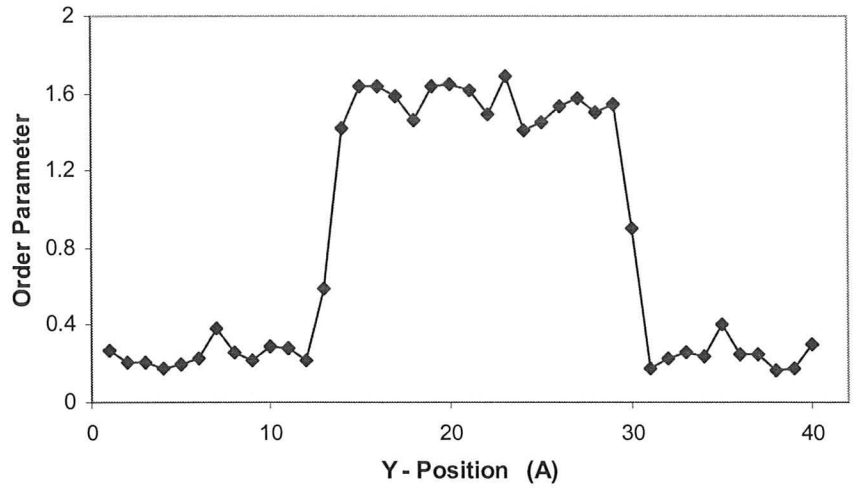

Fig. 3.2: Plot of the order parameter as a function of the position along the interface. The result is collected from the simulation of (110) interface at 915K.

The values of instantaneous fluctuation amplitudes are then computed from the interface height profiles and are averaged over all configurations to yield $\langle |A(k_x,k_z)|^2 \rangle$ from which the stiffness values are extracted. Actually the stiffness values are derived from the least-square fit of a log-log plot of $\langle |A(k_x,k_z)|^2 \rangle$ versus wave vector $|k|$ in accordance with Eq. 3.3 for (100) interface and Eq. 3.4 for (110) interface. The fitting procedure follows exclusion of the data beyond a certain cut-off value at higher $|k|$ at which the stiffness values converge. A plot of the typical fit for (100) oriented interface at

900K is shown in Fig. 3.3(a) which exhibits a deviation of some amplitude values from the fit. The bending trend of the data is suggesting that it could be due to a higher order effect (higher than k^2) in the CFM theory of Eq. 3.2. A similar curvature has been also observed in the study of LJ system[75]. To take into account this higher order correction, the fluctuation data were refitted to a modified analysis of Eq. 3.2. For the (100) interface,

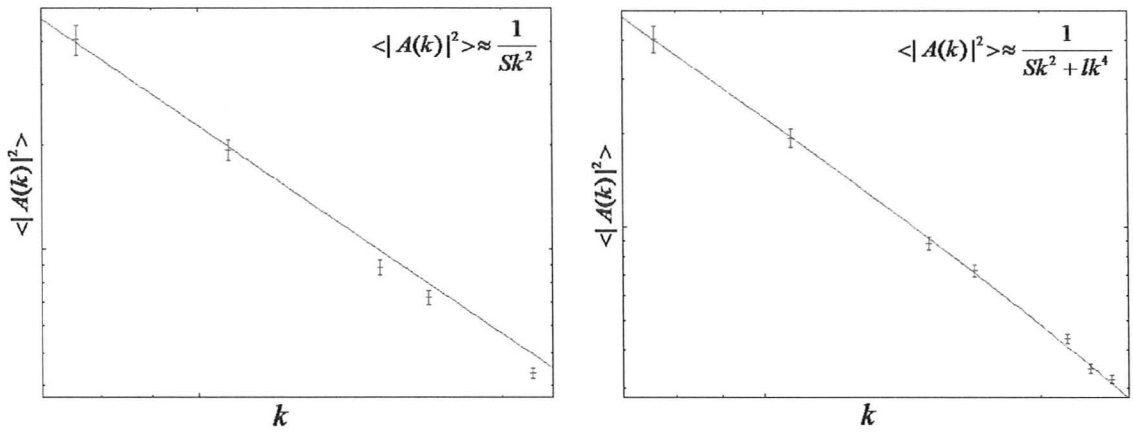

(a) (b)

FIG. 3.3: Fitting of the Fourier amplitude values; (a) without (b) with curvature correction for (100) interface at 900K.

the corrected fitting form was $\frac{1}{(Sk^2 + lk^4)}$ where a symmetrical higher order term, k^4, is added in the denominator[80] and l being a parameter encapsulating the strength of the curvature term. This modified fitted plot is shown in Fig. 3.3(b) for (100) interface at the temperature of 915K. For the (110) oriented interface the modified fit was the form of $\frac{1}{((S_{xx}k_x^2 + mk_x^4) + (S_{zz}k_z^2 + nk_z^4) + pk_x^2k_z^2)}$.

The raw and curvature corrected stiffness values of both the (100) and (110) interfaces for all temperatures are summarized in Table 3.1 and plotted in Fig. 3.4. In the Table 3.1, the numbers in the parenthesis represent the error bar (one σ) on the last digit of the corresponding value. Both the raw and curvature corrected values show the same trend of variation of stiffness with the temperature, but consistently lower values are observed for the latter one for all temperatures. The stiffnesses S and S_{zz} are seen to generally increase with temperature which is consistent with the binary LJ results[75]. The magnitudes S_{zz} stiffness values are observed to be consistently higher than that of S and S_{xx}. The value of S_{xx} stiffness is lower for the pure element than the alloy at the temperature just next to melting point.

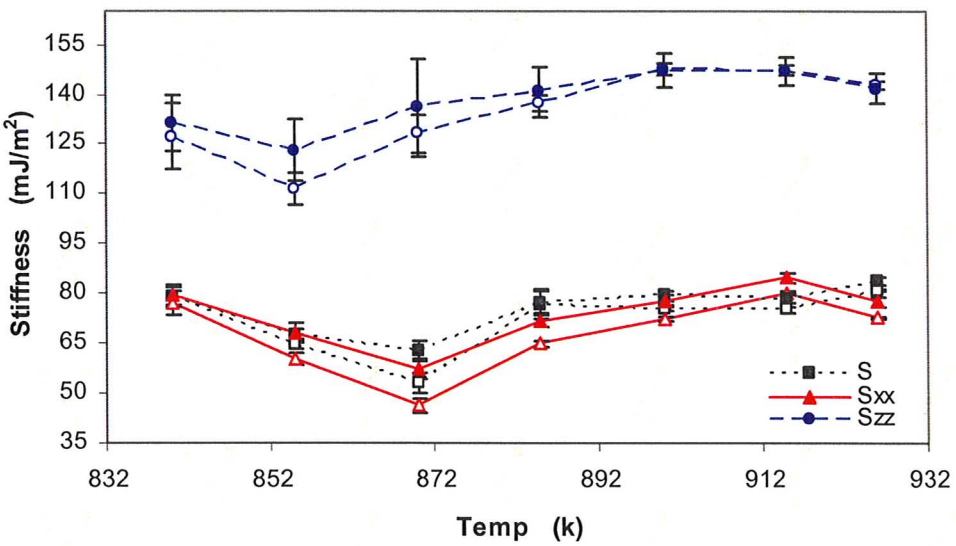

FIG. 3.4: The stiffness values as a function of temperature for (100) and (110) orientations. The open symbols correspond to the raw data and the filled symbols represent the curvature corrected data.

TABLE 3.1: Computed stiffnesses at all considered temperature where S for (100)[010] stiffness, S_{xx} for $(110)[1\bar{1}0]$ stiffness and S_{zz} for (110)[001] stiffness. Stiffness in mJ/m^2.

T	S	$S(curv\_corr)$	S_{xx}	$S_{xx}(curv\_corr)$	S_{zz}	$S_{zz}(curv\_corr)$
840	79(3.2)	79(2.5)	79(3.3)	77(3.7)	131(8.5)	127(9.8)
855	68(1.4)	64(1)	68(3)	60(2)	123(9.2)	112(4.8)
870	63(3)	53(3)	57(2.9)	46(2.1)	136(14.6)	128(5.7)
885	77(3.6)	77(4.3)	72(2.1)	65(1)	141(7.5)	137(2.5)
900	79(1.4)	75(0.6)	78(1.6)	72(0.7)	147(5.2)	147(1.7)
915	79(1.4)	75(0.9)	85(1.5)	80(0.6)	147(4.2)	147(1.4)
926	84(1.1)	81(0.4)	78(1.5)	73(0.4)	142(4.6)	143(1)

3.6 Computation of Interface Energy and Its Anisotropies

The interfacial free energies and their associated anisotropies were then calculated for all temperatures by fitting the stiffness values into the relations derived from Eq.(3.1) for different orientations following the procedure described in Ref. [22]. The equations that relate the interfacial stiffnesses and free energies along with the anisotropy coefficients, developed from Eq.(3.1), are summarized in the following Table 3.2.

TABLE 3.2: The expressions of interface stiffness, $(\gamma+\gamma'')$, in terms of orientationally averaged interfacial free energy, γ_0, and its four fold, ε_1, and six fold, ε_2, anisotropy. The notation (ijk) denotes the interface normal and [hkl] corresponds to the direction.

Stiffness	*Interface*	$(\gamma+\gamma'')$
S	(100)[010]	$\gamma_0\left[1-\frac{18}{5}\varepsilon_1-\frac{80}{7}\varepsilon_2\right]$
S_{xx}	$(110)[1\bar{1}0]$	$\gamma_0\left[1-\frac{21}{10}\varepsilon_1+\frac{365}{14}\varepsilon_2\right]$
S_{zz}	(110)[001]	$\gamma_0\left[1+\frac{39}{10}\varepsilon_1+\frac{155}{14}\varepsilon_2\right]$

The results of orientationally averaged interfacial energy (γ_0) and the surface energy of (100), (110) and (111) are summarized in Table 3.3 where the numbers in the parenthesis refer to the error bar on the last digit of the corresponding value. Fig. 3.5 shows the temperature dependence of γ_0 and the interfacial energy for the other three orientations. Fig 3.5 exhibits the trend of $\gamma_{100} > \gamma_{110} > \gamma_{111}$ at all temperatures which agrees well with the previous simulation results for elemental fcc metals. The interfacial energies display a temperature dependence showing an increase with increasing temperature (i.e. with increasing the concentration of higher melting point material) which is in agreement with that of both Ni/Cu[22], Hard sphere[32] and Lennard Jones systems[75].

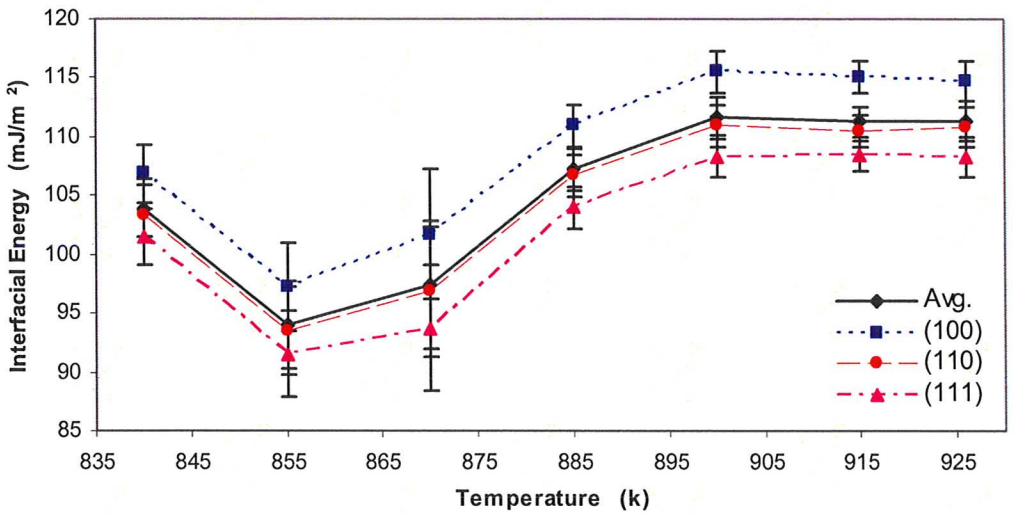

Fig. 3.5: Orientationally averaged interfacial free energy (γ_0) and interfacial energy for (100), (110), (111) orientations as a function of temperature

The average interfacial energy of pure Al obtained here (111 mJ/m^2) is comparable with the γ_0 value 103 mJ/m^2 (considering the uncertainties) obtained by Morris[81] using same Al potential. The magnitude of γ_0 for pure Al calculated in this study is also very close to the value of 108 mJ/m^2 found from nucleation experiments by Kelton[82] and somewhat lower than the value (149 mJ/m^2) computed by Morris[26] from the fluctuation approach of MD simulations using a different Al potential than the one utilized in this study.

TABLE 3.3: Curvature corrected and raw data of orientationally averaged interfacial free energy, γ_{100}, γ_{110}, γ_{111} for all temperatures.

T	γ_0	$\gamma_0(curv\_corr)$	γ_{100}	γ_{110}	γ_{111}
840	104(2.5)	102(3.5)	107(2.5)	103(2.5)	101(2.5)
855	94(3.7)	87(1.8)	97(3.7)	94(3.7)	92(3.7)
870	97(5.5)	89(1.3)	102(5.5)	97(5.5)	94(5.4)
885	107(1.8)	105(1)	111(1.8)	107(1.8)	104(1.8)
900	112(1.8)	110(0.5)	115(1.8)	111(1.8)	108(1.8)
915	111(1.3)	110(0.2)	115(1.3)	111(1.3)	108(1.3)
926	111(1.7)	110(0.3)	115(1.7)	111(1.7)	108(1.7)

The curvature corrected orientationally averaged γ_0 values are compared with that of raw vales in Fig. 3.6. It is found that the resulting values of γ_0 (with curvature) were consistently lower by roughly 5~10% than that of raw data. The temperature dependence of the interfacial free energy remained nearly unchanged. The same effect of curvature was observed in the study of LJ system by Becker[75]. Higher statistical uncertainties on the γ_0 values (both with and without curvature) are observed at low temperatures.

3.7 Solute Adsorption and Excess-Entropy Contributions to Interfacial Free Energy

The Gibbs' adsorption theorem provides a formalism to describe the behaviour of γ as a function of the temperature in a binary system. A complete understanding of the variation of γ with the changes in composition and solute chemical potential μ_{Mg} can be obtained from this theorem. The following equation expresses the temperature dependence of γ according to the Gibbs' adsorption theorem[83]:

$$d\gamma = -S_{xs}dT - \Gamma_{Mg}^{Al}d\mu_{Mg} + (f-\gamma)d\ln a \tag{3.6}$$

where $S_{xs}(=-\partial\gamma/\partial T)$ is the interfacial excess entropy, Γ_{Mg}^{Al} is the adsorption coefficient of Mg with respect to Al, f is the interface stress and a represents the cross sectional area. To analyze the behaviour of $\gamma(T)$ completely, the relative contribution of interface adsorption, excess entropy and the interface stress to γ is required to calculate. Actually f is defined as $\gamma + a\partial\gamma/\partial a$. The cross sectional area is almost kept constant during the simulation, so the change in γ with respect to a is very small in the expression of f. This results in a negligible effect of the third term in Eq. 3.6. So, the interfacial energy depends only on the solute adsorption at the interface and interfacial excess entropy and Eq. 3.6 can be rewritten as:

$$\frac{d\gamma}{dT} = -S_{xs} - \Gamma_{Mg}^{Al}\frac{d\mu_{Mg}}{dT} \tag{3.7}$$

To observe the adsorption contribution, the solute chemical potential (μ_{Mg}) and its temperature dependence is computed as per details in Ref. [75]. The relative

absorption coefficient is defined as the excess amount of solute per unit area relative to that of solvent. The values of Γ_{Mg}^{Al} at the interface is calculated from bulk values of the species densities for solid and liquid phases using the following formulation[42]:

$$\Gamma_{Mg}^{Al} = \frac{1}{2a}\left[N_{Mg} - \left(\frac{\rho_{Mg}^{l} - \rho_{Mg}^{s}}{\rho_{Al}^{l} - \rho_{Al}^{s}} \right) N_{Al} - aL_y \left(\rho_{Mg}^{s} - \left(\frac{\rho_{Mg}^{l} - \rho_{Mg}^{s}}{\rho_{Al}^{l} - \rho_{Al}^{s}} \right) \rho_{Al}^{s} \right) \right] \tag{3.8}$$

where a is cross sectional area of the simulation cell, N_i represents the average number of atoms of species i in the SGC-MC simulation, ρ_i^{α} (atoms per unit volume) denotes the bulk density of species i in α phase, and L_y is the length of simulation cell normal to the interfaces.

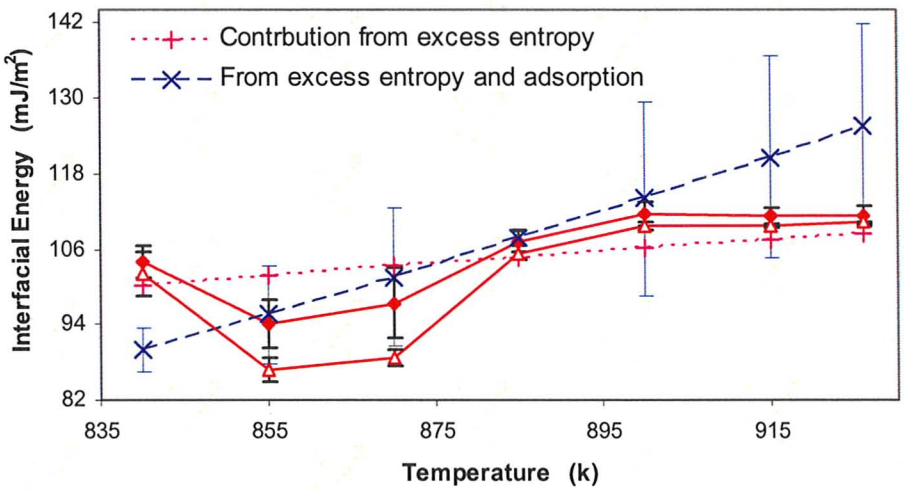

Fig. 3.6: The contributions to interfacial free energy from interfacial solute adsorption and interface excess entropy. The filled symbols are the raw data while the open symbols refer to the curvature corrected values.

In Ref. [75], the analysis of a LJ binary system has shown that the excess entropic contribution accounts for roughly 80% of the γ value for the pure elements while the remaining contribution is attributed to excess enegy. Considering this estimate of S_{xs}, the role of interfacial excess entropy is calculated in this study. The contribution of both solute absorption and excess entropy to interfacial free energy of Al-Mg binary alloy is shown, according to Eq. 3.7, in Fig. 3.6. It is found that both terms have contributions to the temperature dependence of interfacial energy. The excess entropy contribution exhibits an increase with increasing T while the solute adsorption contribution shows the reverse trend. This phenomenon is shown in Fig. 3.6 where the combined contribution from both excess entropy and solute adsorption produces a slope which, with uncertainties, is comparable to the change in γ with temperature. The negative value of excess entropy ($S_{xs} = -\partial\gamma / \partial T$) is found to be consistent with the positive temperature dependence of γ. This large entropic contribution to γ of Al-Mg in the present work is in good agreement with the "neg-entropic" theory of crystal-melt interface by Spaepen[84] which suggests that the negative entropy contribution to $\gamma = E_{xs} - TS_{xs}$ is dominant relative to that of excess energy.

3.8 Prediction of Dendrite Growth Direction in Al-Mg Binary Alloy

In this section the values of the anisotropy parameters of interfacial energy are analyzed for the prediction of possible changes in dendrite growth direction as a function

of solute concentration in the binary Al-Mg binary alloy system. The raw values of four-fold (ε_1) and six-fold (ε_2) anisotropy parameters are given in Table 3.4.

TABLE 3.4: Calculated Four-fold and six-fold anisotropy parameters of interfacial free energy of the Al-Mg system

T	ε_1	ε_2
840	0.076(13)	- 0.0030(13)
855	0.089(16)	- 0.0035(9)
870	0.120(29)	- 0.0063(11)
885	0.094(12)	- 0.0051(11)
900	0.093(8)	- 0.0040(5)
915	0.088(6)	- 0.0021(5)
926	0.084(7)	- 0.0049(5)

The raw values of anisotropy parameters are plotted in the space of ε_1 vs $-\varepsilon_2$ in Fig. 3.7 for all the temperatures studied where these values are superimposed on the orientation selection map, calculated from phase field simulations[33]. The magnitudes of both ε_1 and ε_2 are observed to vary by a considerable amount with respect to temperature which is consistent with that of Lennard Jones (LJ)[31] and Hard Sphere (HS)[32]. This is because the LJ system [shown in Fig. 3.8] with the variation in bond strength between the species shows variation in ε_2 and HS system [Fig. 3.8] with size mismatch affects ε_1 while this Al-Mg binary alloy system with both energy and size mismatch exhibits effect on both ε_1 and ε_2 simultaneously with change in the solute concentrations.

The location of the anisotropy parameters and their changes with respect to composition in the orientation selection map will indicate the orientation of dendrite

growth and the change in growth direction with composition as well. In Fig. 3.8, the LJ system is observed to display growth in the <100> direction for pure element and at the dilute compositions and the trend of change in ε_1 and ε_2 with increasing solute concentration shows a tendency of branching the dendrites in concentrated alloys at around 50% solute. Any increase in concentration afterwards will return the system back

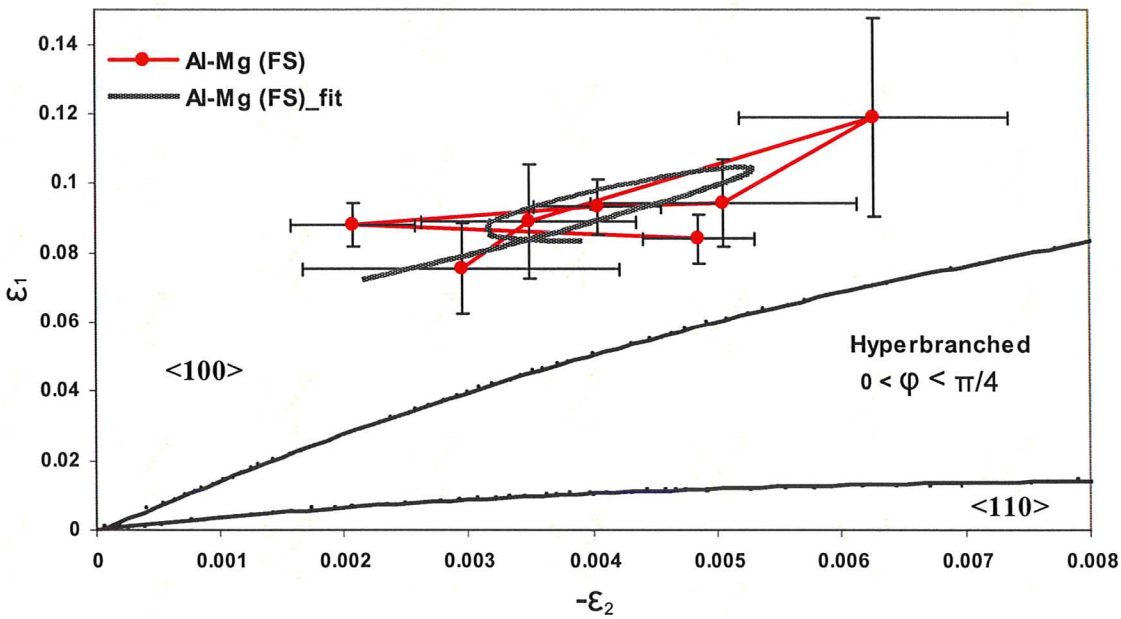

FIG. 3.7: The anisotropy coefficients of interfacial free energy of Al-Mg system (this work) overlaid on orientation selection map.

into the <100> growth region. The arrow of movement in anisotropy parameters for HS system shows <100> growth for the pure element while the tendency will follow a track moving away from the hyperbranched area with solute addition, but the variation in ε_1 is slow for the dilute system. In the case of this model Al-Mg alloy, the anisotropy parameters are found to be located well in the domain of <100> growth region. Starting

from the pure element, the location of these values remains in the <100> region even after increasing the solute concentrations in the system. This suggests that the addition of Mg to Al in Al-Mg binary system tends to stabilize dendrite growth along {100} directions. The black solid line, in Fig. 3.7, shows smooth variation of the anisotropy parameters with solute addition which is obtained by fitting the stiffness values into a polynomial.

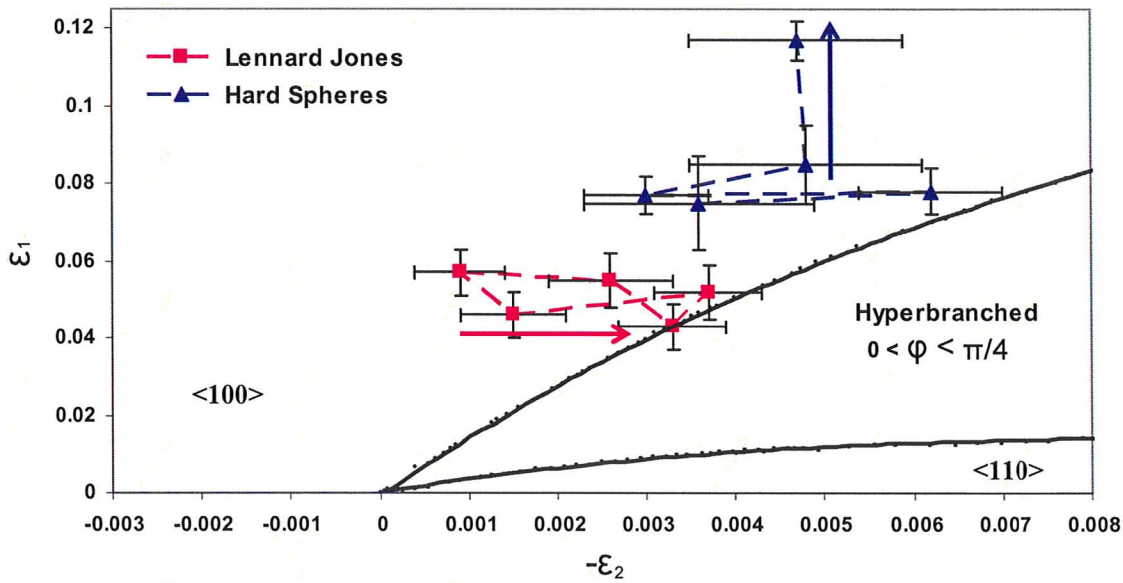

FIG. 3.8: The anisotropy coefficients of interfacial free energy of Lennard Jones (LJ) and Hard Sphere (HS) system overlaid on orientation selection map.

In experimental studies by Henry et al.[85,86], Henry stated that the preferential growth direction of some Al-alloys, including Al-Mg, will switch from <100> to <110> direction. Actually they have conducted directional solidification characterized with high thermal gradient and high solidification rate. Their experimental set up also induced some convection in the melt during crystallization. They attributed their results of change in

growth direction and the observed crystal growth morphology to the local solidification conditions applied in their experimental system. Henry's experimental result of altering the orientation of dendrite growth appears to be in contradiction to the MD results obtained in this study, which indicates that Mg additions to Al will stabilize dendrite growth along (100) directions. There are several possible explanations that can clarify the discrepancy between the experimental and MD results. First, the inter-atomic potential of this model Al-Mg system could play a possible role in this disagreement. Although the potential reproduces well the Al-rich part (the side of our interest) of the phase diagram, it may not be able to capture the subtle trend of change in weak anisotropy parameters as a function of the solute composition.

Second, it is explained in Ref. [85] that the change in dendrite growth direction observed experimentally might be induced by the change in anisotropy of surface energy and/or, the atomic attachment growth kinetics. At higher growth rate, the dominance of the atom attachment kinetics becomes more important and its contribution can modify the preferential growth directions predicted by the anisotropy of γ only. This is because at high speed the anisotropy direction of attachment kinetics (controlled by the anisotropy of kinetic coefficient) may not coincide with that of surface energy. In the present work, the results of dendrite growth orientation that concludes the stabilization of (100) growth of Al with Mg addition is based on an analysis of only the anisotropy parameters associated with interfacial free energy.

Third, from the experiment of Henry et al., the growth morphologies were observed as feathery grains i.e. columnar grains made of twinned dendrites. Besides high thermal gradients and crystallization rates, the melt convection can influence the formation of feathery grains[87]. As described in Ref. [85], the fluid flow favours the spontaneous formation of stacking faults that will lead to the small twinned regions during the growth. The convection of the fluid will then promote the twinned dendrites to grow over the course of solidification. This influence of convection current in the formation of feathery grains is confirmed afterwards by Henry et al.[88]. In Ref. [88], it has been described that the twining was found to start from regions of the melt where the shear flow is highest as strong shear rate is expected to support the occurrence of stacking faults and thus of twins. The experimental investigation of Henry et al. shows that the presence of melt convection triggers the twinning which in turn affects growth of the dendrites in Al-alloys. Hence the mechanism of dendrite growth from Henry's experiment seems to be different than that of our analysis describing a simple change in γ anisotropy due to solute additions. Given the twin assisted growth mechanism of Henry et al. experiments, we can conclude that our results of the stabilization of <100> dendrite growth direction for Al-Mg alloy with Mg addition is not unreasonable.

CHAPTER 4

Kinetic Coefficient of Crystal-Melt Interface

The kinetic coefficient (μ), also called the interface mobility, is defined as the constant of proportionality between the growth velocity (V) of solid-liquid interface and the interface under-cooling [$\Delta T = T_M(P) - T$]:

$$V(T) = \mu \Delta T \qquad (4.1)$$

where T_M is the zero pressure melting point. The interface mobility is known to be a crucial factor for controlling the kinetics of isothermal crystallization and melting. Actually both the magnitudes and associated crystalline anisotropy can play a dominant role in governing the crystallization rates and growth morphologies at large under-cooling which corresponds to rapid solidification[89-94]. Recent work by Bragard et al.[94] has shown that the anisotropic values of kinetic coefficient are critical parameters in phase field modelling of dendritic solidification.

4.1 Literature Review of Crystallization Kinetics

Due to the inherent difficulties associated with direct experimental measurement of kinetic coefficient, to date only a few studies[95-96] have attempted to measure this parameter. The anisotropic behaviour of μ was not considered in those approaches. The

lack of experimental measurement leads the way of atomistic simulation techniques to come into play. Much of the current theoretical understanding of crystal-melt interface kinetics has been derived from atomic scale Molecular Dynamics (MD) and Monte Carlo (MC) simulations[15,19,21,24-25, 97-115].

In 1982, Broughton, Gilmour and Jackson presented the first crystal-growth simulation model for Lennard-Jones (LJ) system[97]. Actually the model of Broughton *et al.* was emerged as a pioneer MD work and known as BGJ model. This model provided some important insights of the atomic scale process that corresponds to the underlying crystallization kinetics of the molecularly rough interface. They showed that the LJ system can be described by a collision limited growth model in which growth of the interface depends on the frequency of collisions of liquid atoms to the crystal interface. This model was found to be inconsistent with earlier transition-state theories of crystallization kinetics in which the atom attachment to the growing interface is described as a diffusion limited process[112, 116-118] which is illustrated in the thermal activation model of Wilson and Frenkel (WF)[117-118]. The results of BGJ model contradicted the diffusion limited WF model, because BGJ produced considerable growth rate even at very low temperatures where the liquid diffusivity is negligible. But the BGJ model was in good agreement with the observations of Turnbull and his co-workers[119,120], who first suggested the growth kinetics of elemental metals as being "collision limited".

But the main draw back of the BGJ model was that they didn't consider the effect of crystalline anisotropy in their description of crystallization kinetics. BGJ model has

been interpreted[19] to predict the anisotropy dependence of kinetic coefficient in terms of the differences in inter-planar spacing (d_{ijk}/d_{lmn}) for the interfacial orientation of (ijk) and (lmn). On the basis of this thought, BGJ model would predict that $\mu_{111}>\mu_{100}>\mu_{110}$ for the materials of fcc crystal structure. This prediction is observed to be in well agreement with the results of (100) and (110) interfaces as the ratio of μ_{100}/μ_{110} is often observed to be close to the d spacing ratio of $\sqrt{2}$. But, for the (111) oriented interface, μ_{111} is found to have the smallest value[19] among all the three interfaces which is contradictory to the prediction by BGJ model. The slower growth in (111) interface for fcc systems has been explained by Burke et al.[98] and they attribute the reason to formation of the transient hcp stacking faults during the crystallization process. The defective HCP islands may form during the solidification of the system with lower stacking fault energy (SFE) which must be annealed out for the crystallization to take place. The annealing process of the HCP islands slows down the interface growth rate.

Although, the lower SFE systems are sensitive to the formation of HCP atoms at the S/L interface, the slower growth of (111) interface was also found in the systems with higher SFE[25]. An alternative framework that yields the predictions concerning crystalline anisotropy of kinetic coefficient is the growth model introduced by Mikheev and Chernov[121] within the formulation of kinetic density-functional theory (DFT). This model is based on a diffuse crystal-melt interface at atomic level. The Mikheev-Chernov model appears to be in close agreement with some recent simulation results[25] for the anisotropy in interfacial mobility of the system with high SFE.

4.2 MD Simulation Techniques for Computing Interface Mobility

To date several Molecular Dynamics simulation techniques have been developed and employed to determine the kinetic coefficient of the solid-liquid interface. These techniques can be categorized as forced velocity simulations, free solidification, imposed pressure simulations and fluctuation analysis. In the present research work, a detailed study of *free solidification method* (FSM) and *capillary fluctuation method* (CFM) have been undertaken to compute and analyze the interface mobility and its associated anisotropy of pure Al. In FSM[97,100,21,25,114], the solid-liquid system is first equilibrated at the melting point which is then simulated at a variety of different undercoolings. During the solidification, the interface movement is monitored through the track of the total energy which leads to the determination of growth velocity (V) as a function of undercooling (ΔT) and eventually μ is calculated using Eq. 4.1. In CFM[15,114], the equilibrium fluctuation of crystal-melt interface is analyzed and μ is extracted from the measurement of interface height as a function of relaxation time of the fluctuation spectra. The detailed analysis of the FSM is presented in this chapter while the CFM analysis is described in the following chapter.

4.3 Free Solidification Method (FSM)

The free solidification method (FSM) is a non-equilibrium MD (NEMD) simulation approach used to derive kinetic coefficient. The FSM technique involves a crystal-melt system where the solid and liquid region is separated by a solid-liquid (S/L)

interface with periodic boundary conditions. Initially, the middle region of the simulation cell is melted which is followed by the equilibration of the liquid part of the system at T_M. Then the entire system is equilibrated at the melting point. The resulting simulation cell is composed of two S/L interfaces containing solid regions at the both ends and a liquid phase region at the middle.

The FSM procedure starts with the application of a constant temperature field to the system which is below the melting point ($T<T_M$). This MD simulation is performed in the NAP_zT ensemble where only the dimension normal to the interface is allowed to move to accommodate the associated volume changes in the system in order to maintain zero pressure in that direction. The cross sectional area of the simulation cell, a, is kept constant during the whole procedure to ensure a strain free system while the imposed temperature is maintained by using the Nosé-Hoover thermostat. The applied temperature will cause the system to solidify at that specific undercooling. The movement of the solid-liquid interface with time is observed by tracking the total potential energy (PE) of the system as described in detail in Ref. [107]. The velocity of interface growth is then calculated from the slope of PE/atom vs. simulation time plot.

4.4 Kinetic Coefficient Measurement of Pure Al From FSM

In this research work, kinetic coefficient of pure Al is measured for the (100) and (110) oriented crystal growth interface. The free solidification simulation is performed on $20 \times 20 \times 40$ (unit cells) simulation cells containing 64000 atoms for the (100) interface

simulations and on $20 \times 14\sqrt{2} \times 28\sqrt{2}$ (unit cells) simulation cells containing 62720 atoms for the (110) interface runs. The solid-liquid system is created by melting the middle ½ of the simulation cell along the z direction at a temperature above the melting point. Actually we have applied 1700K (T_M = 926K) to the middle part for melting while the solid atoms at both ends are kept fixed. The liquid region is then equilibrated at T_M which is followed by the equilibration of the entire system at the melting point. During the runs of equilibration, the evolution of pressure, energy, volume and temperature was monitored to check for steady state. Finally, the system is run in a constant energy ensemble to obtain an equilibrium system with coexisting solid and phase.

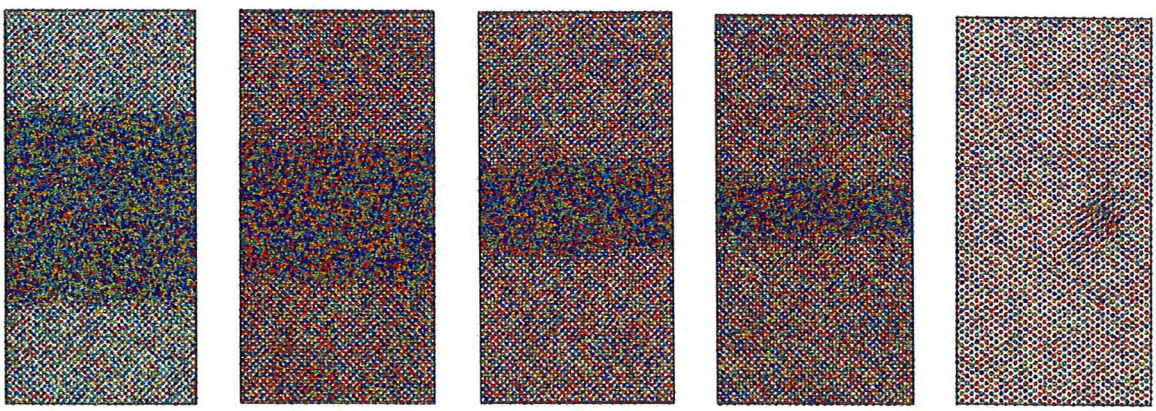

Fig. 4.1: Some snapshots of the simulation cell representing the crystallization process with time for (110) oriented interface at 5K undercooling employing the FSM technique

To cause movement of the interface, in total six different temperatures are applied to this equilibrated solid-liquid system for both (100) and (110) interfaces where three temperatures were below the melting point and the other three were above T_M. For the

temperature field of $T<T_M$, subsequent solidification takes place with time which is shown in Fig. 4.1 in terms of some snapshots taken during the simulation of (110) oriented interface at 5K under-cooling. During the phase transition period, the interface growth is monitored through change in the total potential energy (PE) of the system which is observed to decrease with time accompanying the growth of the crystal. The profile of total PE of the pure Al system during crystallization of (100) interface at 15K undercooling is shown in Fig. 4.2 as a function of simulation time. In contrast, the temperature field of $T>T_M$ is followed by subsequent melting which increases the PE of the system with time due to the associated growth of the liquid phase and interface movement is observed accordingly.

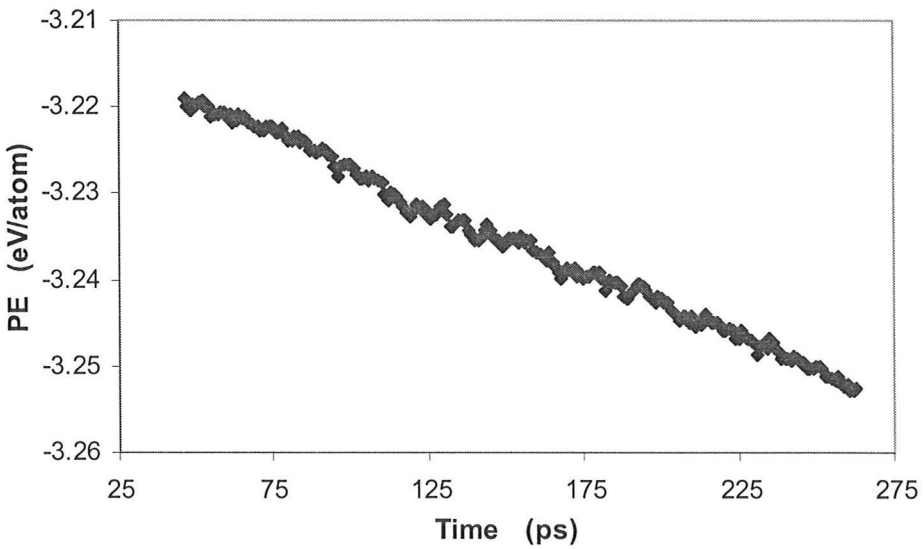

Fig. 4.2: PE/atom as a function of time during free solidification for (100) oriented interface at 15K under-cooling

The solid-liquid system in the free solidification method is characterized with two constraints. The total number of atoms is the summation of atoms in the liquid phase and that of solid phase ($N_T = N_S + N_L$). The potential energy (PE) of entire system would be the linear combination of weighted PE of both phases ($N_T E_T = E_S N_S + E_L N_L$). Utilizing these two constraints, the equation for growth velocity has been developed which is:

$$V(\Delta T) = \frac{\dot{E}\, N_T\, V_s}{2a(E_l - E_s)} \tag{4.2}$$

where $\dot{E}$ is the slope of PE/atom vs. time plot, N_T is total number of atoms in the system, V_s is volume/atom of the bulk solid (fcc) phase at T_M, a is cross sectional area of the simulation cell, E_l and E_s represent the PE/atom of the bulk solid and liquid phases respectively at T_M. The '2' in the denominator of Eq. 4.2 represents the two S/L interfaces in the simulation cell. Then the growth velocity (V) is calculated at each temperature for both the (100) and (110) oriented interfaces utilizing Eq. 4.2 by extracting the slope from PE/atom vs. time plot.

TABLE 4.1: The growth velocity as a function of temperature for (100) interface

Temp (K)	Interface Velocity (cm/s)
911	- 1184.4
916	- 736.4
921	- 404.42
931	404.62
936	681.7
941	1064.2

For all temperatures, above and below melting point, two independent simulations are performed and the average interface velocities are calculated. Table 4.1 summarize the average growth velocities for (100) oriented interfaces. Then the slope of the interface growth velocity vs. temperature plot provides the magnitude of the kinetic coefficient. This plot of (100) oriented interface is shown in Fig. 4.3 where the solid line in the plot is the fit to a linear relationship. We found for pure Al, the kinetic coefficient for (100) oriented interface is $\mu_{100} = 75 \pm 11$ cm/s/K and for (110) oriented interface is $\mu_{110} = 62 \pm 8$ cm/s/K.

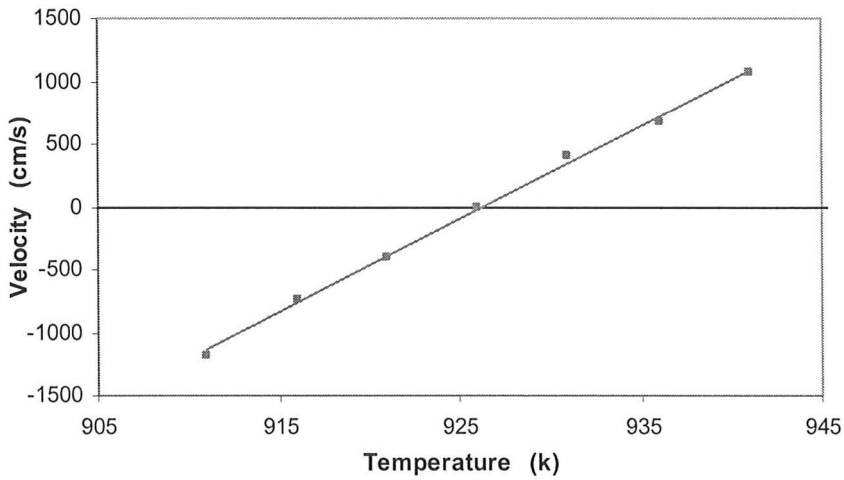

Fig. 4.3: Interface growth velocity as a function temperature for (100) oriented interface

4.5 Problem of the Single Thermostat FS Method

In the free solidification method, a single global thermostat at known undercooling is employed to crystallize the solid-liquid system. The associated phase transformation from liquid to crystal causes generation of latent heat in a local region

surrounding the interface and this heat has to be dissipated in the system rapidly during the course of simulation to keep the interface at the thermostat set point temperature. Actually in the case of classical Molecular Dynamics technique the only contribution to the diffusion of heat comes from the atomic vibration as there is no involvement of electrons. Hence heat dissipates very slowly and the rate of heat diffusion competes with the rate of atom attachment to the growing crystal. The slow heat dissipation in fact increases the temperature at the crystal-melt interface. Fig. 4.4 shows a non-uniform temperature profile during the free solidification of a pure Ni system[122] illustrating a peak at the position of interface. In this example, the thermostat was applied at T = 1690K with 20K (T_M = 1710K) under-cooling (horizontal dashed line). In the figure, dotted lines denote the profile from three independent snapshots while the solid line is their average.

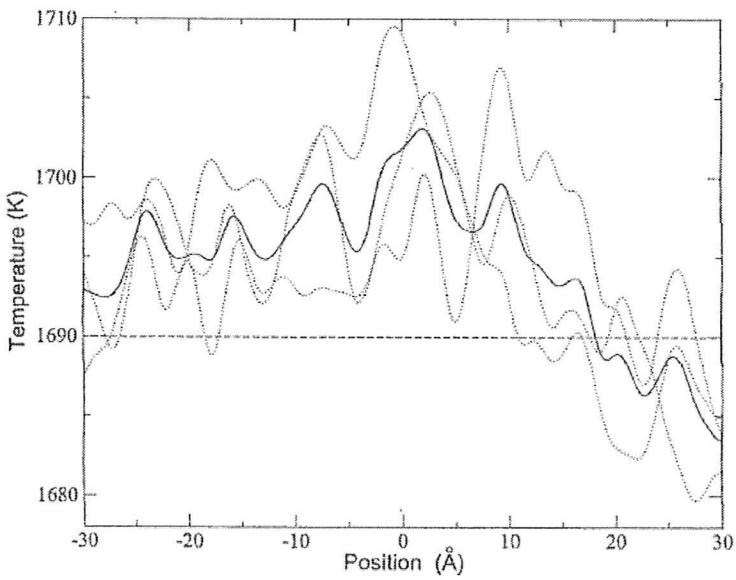

Fig. 4.4: The temperature profile across the crystal-melt interface during the crystallization of Ni system in Ref [122].

To maintain the entire system at a specified applied temperature, the global thermostat decreases the temperature below the set point value as a compensation to the spike in interfacial temperature. The phenomenon of increasing temperature at the interface actually sets a lower undercooling than the applied one for the growth of interface during the course of solidification. This leads to a slow growth of the S/L interface and hence extraction of the interface mobility from the applied undercooling eventually underestimates μ as it relates the growth velocity to the interfacial undercooling. In Fig. 4.4, at the interface position the real undercooling $\Delta T = 10K$ while the thermostat set point is $\Delta T = 20K$ and the temperature falls off below ΔT in the bulk liquid corresponding to the right in the figure. If the thermostat temperature is corrected by the peak temperature at the interface boundary, an accurate value of μ can be obtained. Due to the problem of the spike in interface temperature in a single global thermostat FSM, an alternative method is required for maintaining the proper temperature control during the simulation so that the generated latent heat can be dissipated efficiently. Such a technique will be discussed in the following section.

4.6 Multi-layered Free Solidification Technique

To overcome the heat flow problem, Monk et al.[122] introduced an improved technique of free solidification method where the simulation cell is divided into several sub-regions, aligned normal to the crystallization direction of the solid-liquid interface, and each region is thermostatted independently to a desired under-cooling to control the temperature. The simulations are performed in NVT (fixed total number of atoms, volume

and temperature) ensemble while free surfaces are implemented along the direction (z–axis) normal to the interface for relaxing the pressure of the system. To control the temperature of each bin, velocity rescaling thermostat is employed which resets the temperature of the atoms of each sub-region by explicitly rescaling their velocity. The multilayered free solidification method is just a modified version of FSM in terms of the temperature controlling system.

For the layered free solidification technique, the same geometry of the simulation cell with same number of atoms as in the single thermostat FSM are utilized to determine the kinetic coefficient of (100) and (110) oriented interfaces of pure Al. The interface velocity is computed in the same way as described for the single thermostat FSM technique in Section 4.4 following Eq. 4.2. Then the value of μ is extracted from the slope of growth velocity vs. interface temperature plot. Fig. 4.5 and Fig. 4.6 summarize the plot of growth velocity as a function of interface temperature comparing the multiple and single thermostat free solidification method for both (100) and (110) oriented interface of pure Al respectively.

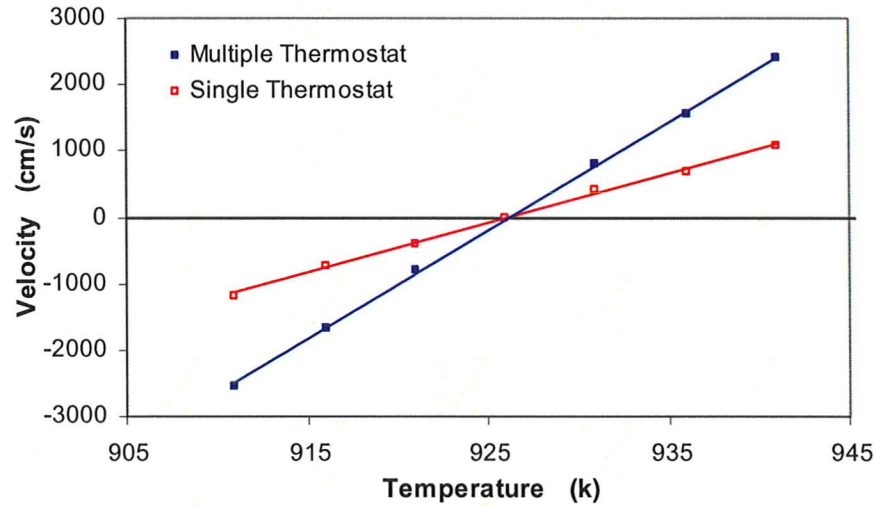

Fig. 4.5: The crystallization velocity vs. interface temperature for (100) oriented interface from multiple and single thermostat FSM

A linear relationship between the growth velocity and interface temperature is observed in both solidification techniques. Fig. 4.5 shows that the interface growth rate is much higher in the multiple thermostat FS technique than that of single thermostat which is consistent with the result of Ni[122] system. The increase in the number of thermostats will reduce the number of atoms to be controlled per thermostat. Hence the amount of generated latent heat to be controlled by each thermostat would be lesser compared to the case of single thermostat for the entire system. This will facilitate the heat to be dissipated away from the interface on a time scale which would be faster than that of single global thermostat. So, the efficient diffusion of heat from the crystal-melt boundary will not increase the interface temperature and it would remain almost the same as the specified set temperature. This will eventually lead the system to overcome the underestimation of kinetic coefficient and we found a higher value of interface mobility in the case of

multiple thermostat. The values of kinetic coefficient obtained from multiple and single thermostat FS techniques for both (100) and (110) interfaces of pure Al are given in the Table 4.2.

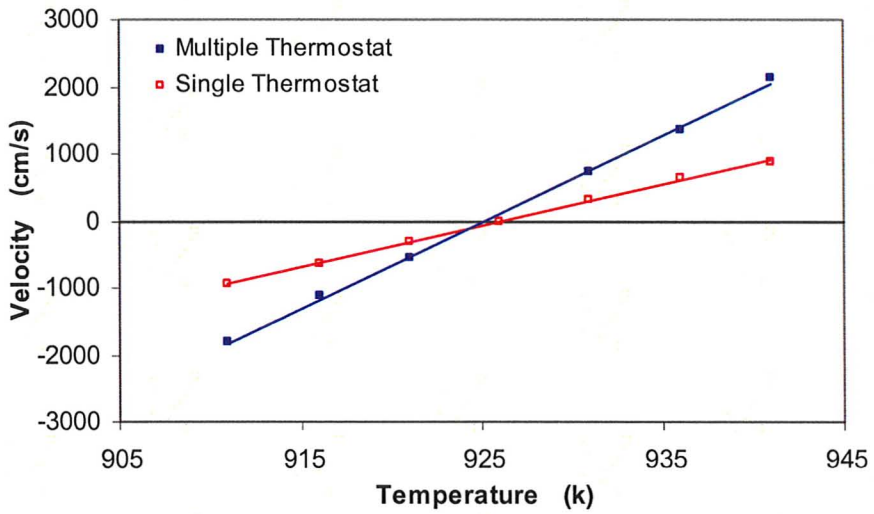

Fig. 4.6: The crystallization velocity vs. interface temperature for (110) oriented interface from multiple and single thermostat FSM

TABLE 4.2: Kinetic coefficients of pure Al for (100) and (110) orientation from FSM. The values in the parenthesis refer to the uncertainties on the last digits.

Interface orientation	Layered FS technique	μ cm/s/K
100	single	75(11)
	multiple	163(15)
110	single	62(8)
	multiple	129(16)

The results of layered thermostat approach for pure Al from this study are observed to be in good agreement with several MD works in elemental metals in two aspects. One is the inequalities among the anisotropic values of kinetic coefficient where the order follows the trend of $\mu_{100} > \mu_{110}$. The other is the ratio of anisotropic magnitude of the interface mobility μ_{100}/μ_{110} which lies between the range of around 1.3 and 1.4 (considering the uncertainties on the μ values for the both crystallographic orientations).

CHAPTER 5

CFM Analysis of Interface Mobility

The interface mobility can be determined by employing an analysis of the equilibrium fluctuations of solid-liquid interfaces utilizing the capillary fluctuation method (CFM). Such equilibrium procedures involve the extraction of the kinetic coefficient from the dynamics of interface fluctuations, instead of the measurement of growth velocity as a function of interfacial under-cooling for NEMD methods. This alternative technique provides an independent check of μ values derived from the non equilibrium Molecular Dynamics (NEMD) methods. This chapter will discuss the detailed analysis of this equilibrium method providing a simple correction due to the contribution of heat flow controlled interface fluctuation. The focus of the mobility calculation in this study is to observe the equivalence of the two computational techniques (FSM and CFM).

5.1 The Analysis of Capillary Fluctuation Method

In the CFM approach, long MD simulation runs are performed in a micro-canonical ensemble to obtain several snapshots of the equilibrium solid-liquid system. The position of crystal-melt interface is determined using the order parameter technique

as described in Section 4.6. The CFM approach makes use of time dependent measurements of the amplitude of sinusoidal interface perturbation to extract the value of μ. The interface fluctuation shows a exponential decay with time and this relaxation, characterizing the dynamics of fluctuation spectra, is governed by the following kinetic equation[123]:

$$< A(k,t)A^{*}(k,0) > = <| A(k) |^{2} > \exp(-t/\tau) \qquad (5.1)$$

where τ refers to the relaxation time, $A(k,t)$ is the Fourier transform of the interface height and $A(k,0)$ represents the reference amplitude evaluated at some arbitrary time. The angular denotes bracket configurational averaged value of the quantity. The relaxation time is related to the kinetic coefficient by $\tau = (\Gamma \mu k^{2})^{-1}$ where Γ is the capillary length and is given by $\Gamma = (\gamma + \gamma'')T_{M}/L$. The quantity $(\gamma + \gamma'')$ is the interfacial stiffness defined in terms of interfacial free energy γ and its double derivative with respect to the angular difference between growth direction and interface normal, T_{M} is the melting point and L is the latent heat per unit volume.

The relaxation time is calculated for each value of k by fitting the exponential decay of time autocorrelation function of $A(k,t)$ according to the Eq. 5.1. The configurational averaged Fourier amplitude of the fluctuating interface, $<| A(k) |^{2} >$, is related to the interfacial stiffness by means of the capillary theory[20]. Therefore, it is most convenient to extract the kinetic coefficient (μ) from a slope of the plot of $<| A(k) |^{2} >$ vs. τ in relation to the following expression[19]:

$$<| A(k) |^2> = \left[\mu \frac{k_B T_M^2}{a L} \right] \tau \qquad (5.2)$$

where a denotes the cross sectional area of the simulation cell.

5.2 The Heat-Flow Problem and Its Correction

In the equilibrium fluctuation technique, crystallization of the liquid phase and melting of the solid phase are taking place continuously at the crystal-melt interface during whole course of the simulation. The kinetics of interface fluctuations is not immune to the slower heat diffusion due to the absence of electronic contribution to thermal transport in classical MD. As the heat can not be dissipated fast enough from the solid-liquid interface, the heat flow will play an important role in establishing the fluctuation spectrum. So, a competition between the heat flow controlled and the atomic attachment controlled interface fluctuation exists there. The slowly dissipated heat will contribute a part in controlling the decay rate of fluctuation amplitudes. In a detailed study of such phenomenon, Karma[123] has demonstrated that the fluctuation spectrum of long wavelength amplitudes (low k) will be controlled by the heat flow kinetics such that an approximate expression for the relaxation time is given by :

$$\tau_1 = \frac{L}{2cD_T\Gamma} \frac{1}{k^3} \qquad (5.3)$$

where c is specific heat per unit volume, D_T is thermal diffusivity, L is the latent heat, and Γ is the capillary length. On the contrary, at high k limit the relaxation time is

dominated by the atomic attachment kinetics and is given by $\tau = \frac{1}{\mu \Gamma k^2}$. Actually Eq. (5.1) is derived under the assumption of k^{-2} dependence of the relaxation time. As the power law behaviour of the k dependence of relaxation time varied in two different k regime, there exists a crossover wavelength, given by $\lambda^* = 4\pi c D_T / (\mu L)$, at which the interfacial fluctuations are equally affected by both the atom attachment and heat flow contributions. Actually, in Molecular Dynamics, the atom attachment kinetics dominated region is valid (corresponding to k^{-2} dependence of the relaxation time) due to the cell geometry typically utilized in the MD simulations.

In a recent analysis, Monk *et al.*[122] have shown that there might be a small contribution from thermally controlled kinetics to the fluctuation spectra determined from MD. Monk and his co-workers have suggested that this contribution can cause an underestimation of the interface mobility in the fluctuation analysis compared to the μ obtained from the layered thermostat free solidification approach. To overcome this problem, an approximate improved fluctuation technique is introduced in Ref. [122] where a correction has been made for the heat flow contribution to the fluctuation kinetics. The corrected fluctuation analysis was found to yield a value of μ consistent with that of non-equilibrium layered free solidification MD technique. In this study, we have applied the heat flow correction, proposed by Monk *et al.*, to the fluctuation spectra of the crystal-melt interface of pure Al system to determine the kinetic coefficient for both the (100) and (110) oriented interfaces.

As described in the earlier section, the time correlated function of interface height $< A(k,t)A^*(k,t=0) >$ relaxes exponentially with time and the relaxation time (τ) is extracted by fitting this decay function. The values of relaxation time for the (100) oriented interface are plotted on the log-log scale as a function of the k vector in the Fig. 5.1 where the solid line refers to the fit of the k^{-2} dependence according to the Eq. (5.1) and the error bars represent the standard deviation. Actually the error bars on τ is calculated by dividing the entire time sequence of 12000 configurations of the crystal-melt interface into 12 sub-regions. Then relaxation time is calculated for each sub-section and eventually the error bars are extracted from the standard deviation of the τ values from these 12 samples. At the high k regime, there is some scatter in the data where relaxation times are small in magnitude, on the order of less than 1ps. Actually, the low τ values at high k (small wavelength) are less reliable as the fluctuation analysis is valid for large wavelength corresponding to high τ values.

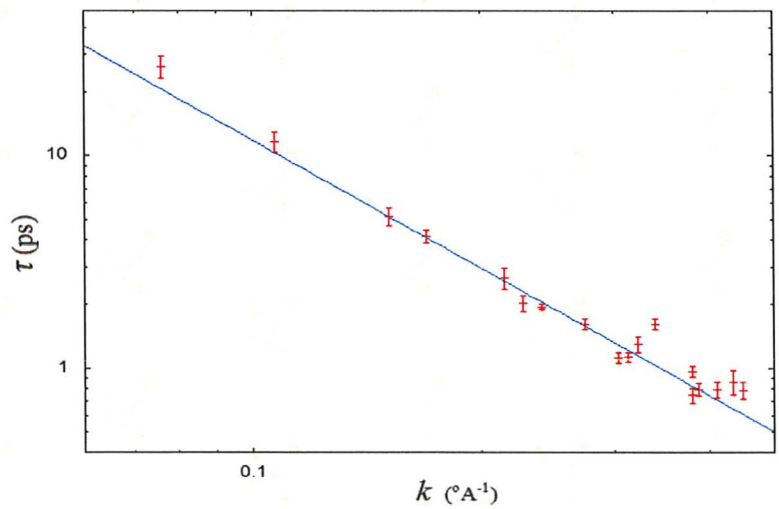

Fig. 5.1: Plot of the relaxation time for (100) interface as a function of wave vector

At the low k region, the values of relaxation time exhibit a small amount of deviation from the fit denoted by solid line. The significance of this small deviation can be attributed to the low thermal conductivities (K) of classical MD. Due to the low value of K, the generated latent heat will not be diffused fast enough from the crystal-melt interface compared to the attachment of the atoms to the interface. The slow heat dissipation will contribute a considerable effect on the decay rate of fluctuation amplitudes in the low k region (long wavelength) where the CFM analysis is applicable. As mentioned earlier, from the analysis of Karma[123], an approximation of the heat flow controlled relaxation time is given by Eq. (5.3) for long wavelength fluctuation amplitudes. The expression of τ_1 in Eq. (5.3) can be written as $\tau_1 = \frac{L}{2K\Gamma}\frac{1}{k^3}$ because the product of specific heat per unit volume (c) and thermal diffusivity (D_T) gives thermal conductivity (K) per unit volume. To quantify τ_1, K is required to be computed.

In Ref. [122], on the basis of Karma's study, Monk *et al.* made an approximation to modify the CFM analysis with correct fluctuation spectrum to obtain more accurate value of the interface mobility. According to the modified analysis of fluctuation technique, the contribution given in Eq. (5.3) is subtracted from the relaxation times derived from the equilibrium MD simulations and the kinetic coefficient is calculated from the corrected relaxation times. This simple adjustment of subtracting the effect of heat flow, suggested by Monk and his co-workers, is an approximation while the actual fluctuation spectra is more complicated than that which is illustrated in detail in Ref.

[123]. To extract the value of τ_1 using the Eq. (5.3), thermal conductivity of the pure Al is computed from classical MD which is described in the following section.

5.3 Thermal Conductivity Calculation for pure Al

The thermal conductivity for the both solid and liquid phases of pure Al is computed utilizing a MD method developed by Muller-Plathe and Reith[124]. This technique is briefly discussed here. The simulation cell is divided into several bins of identical thickness which are oriented perpendicular to long dimension of the cell (z direction) and the system is employed a micro-canonical ensemble. The velocity of the coldest atom in the hottest bin (center bin) is swapped with the velocity of the hottest atom in the coldest bin (edge bin) of the cell at each time step during the whole course of simulation. This mechanism produces an exchange of kinetic energy between the two working slabs which leads to a temperature difference in those bins leaving a temperature gradient in the intervening region. After reaching a steady state, the system will establish a heat flux in response to the imposed energy transfer due to the velocity exchange.

The thermal conductivity (K) can be derived from the induced thermal gradient remaining in the steady state of the system. Actually, the heat flux will be affected by thermal conductivity in such a way that the higher K is, the more efficient the heat transport would be and hence the smaller the temperature gradient will be resulted. The thermal conductivity is calculated using the following equation[125]:

$$K = -\frac{\sum_{transfers} \frac{m}{2}(v_h^2 - v_c^2)}{2\,t\,L_x L_y \left\langle \frac{\partial T}{\partial z} \right\rangle} \tag{5.4}$$

where the summation term refers to the amount of total exchanged kinetic energy taken over all transfers during the simulation time t and v_h and v_c denotes the velocity of interchanging hot and cold atoms of identical mass m respectively. In Eq. 5.4, L_x and L_y are the box length of that area through which the heat is transported and $\left\langle \frac{\partial T}{\partial z} \right\rangle$ represents the ensemble averaged temperature gradient term. At the melting point, we find the value thermal conductivity of the solid phase to be 1.32 ± 0.12 W/m-K and for the liquid phase 0.75 ± 0.05 W/m-K pure Al, which are observed to be around 160 ~ 170 times lower than that of experimental results at the same temperature.

This technique of computing thermal conductivity is known as reverse non-equilibrium MD (reverse NEMD) approach. This is because the conventional NEMD method applies the temperature gradient on the system and the heat flux is measured as a result. In contrast, the Muller-Plathe approach proceeds in the reverse direction where the heat flux is imposed and the temperature gradient is a response from the system.

5.4 Measurement of Interface Mobility from CFM

The fluctuation data of the crystal-melt interface generated to compute the interfacial free energy are also utilized to determine the kinetic coefficient employing the

fluctuation analysis technique for this case of pure Al. Actually, the interface mobility is extracted from slope of the $<|A(k)|^2>$ vs. τ plot as discussed earlier in section 5.1 according to Eq. 5.2. These plots from both raw and corrected (for the effect of heat flow) τ values are shown in Fig. 5.2 and Fig. 5.3 for (100) and (110) oriented interfaces respectively.

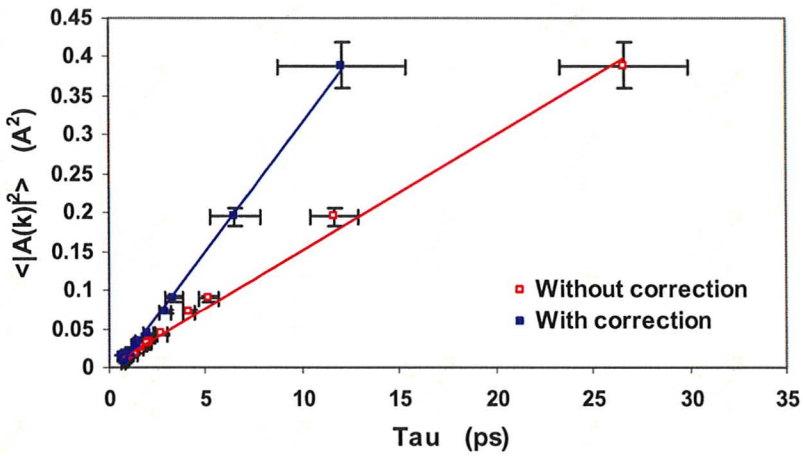

FIG. 5.2: Fourier transform amplitude $<|A(k)|^2>$ vs. relaxation time τ for (100) oriented interface from the fluctuation analysis of crystal-melt interface of pure Al

The values of the kinetic coefficient for both (100) and (110) interfaces are summarized in Table 5.1. In Fig. 5.2, from the slope of the plot for the raw values of τ a kinetic coefficient of $\mu = 89$ cm/s/K is obtained, but application of the heat flow correction increases the value of μ to 192 cm/s/K. This value along with the error bars is found to be in good agreement with that of multiple thermostat FS method. For the (110) oriented interface, the corrected value of μ is also observed to be higher in magnitude

than that of raw data (Table 5.1) and converged with that of layered FS method with the uncertainties. Table 5.1 includes the kinetic coefficient values obtained from layered FSM technique.

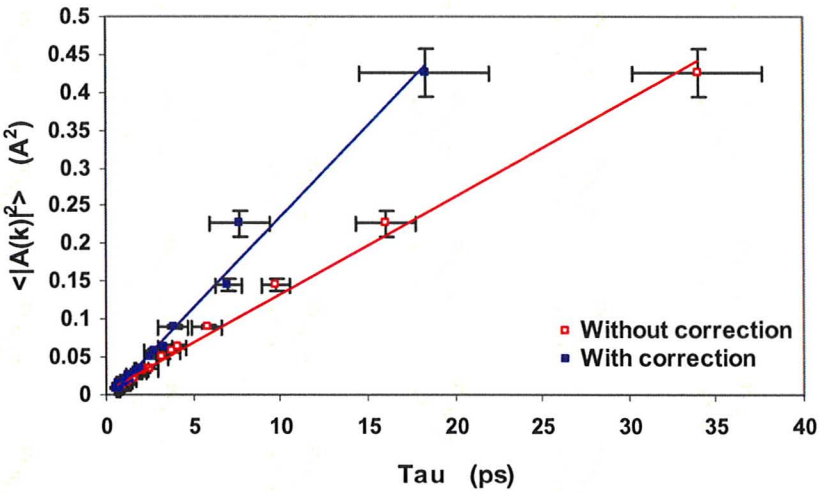

FIG. 5.3: Fourier transform amplitude $<|A(k)|^2>$ vs. relaxation time τ for (110) oriented interface from the fluctuation analysis of crystal-melt interface of pure Al

TABLE 5.1: Kinetic coefficients of pure Al for (100) and (110) oriented crystal-melt interface from the Fluctuation Analysis compared with layered FSM

Interface orientation	Fluctuation analysis	μ cm/s/K	Layered FSM, μ (cm/s/K)
100	Without correction	89(9)	163 (15)
	with correction	192(30)	
110	Without correction	75(7)	129 (16)
	with correction	140(23)	

CHAPTER 6

Conclusion

In this research work, a model Al-Mg system is studied to compute its solid-liquid interface (SLI) properties along with their anisotropies utilizing atomistic simulation techniques such as Molecular Dynamics (MD) and Monte Carlo (MC) simulations. The Al-Mg system is characterized by size mismatch and variation in bond strength between the solvent and solute species. The conclusions that have been drawn from this study are summarized in the following way:

1. An inter-atomic potential of Finnis-Sinclair format for a model Al-Mg system is optimized by comparing the equilibrium Al-Mg phase diagram and liquid enthalpy of mixing determined from this potential (employing Monte Carlo simulations) with those of the experimental results. The MC simulation provides an equilibrium solute composition corresponding to an imposed chemical potential difference between the species at each temperature.
2. The Al-rich side of temperature-composition Al-Mg phase diagram has been determined using thermodynamic integration technique. The solidus and liquidus composition is calculated from the intersection of grand potential functions of solid

and liquid phases. Good agreement is found for the solidus and liquidus lines calculated from this potential with that of experimental phase diagram up to ~ 16% Mg in the liquid phase which corresponds to a temperature of 840K.

3. The liquid enthalpy of mixing obtained from this potential for the Al-Mg alloy is observed to be comparable with those of other experimental results.

4. A miscibility gap is also observed in the phase diagram for this potential after 16% of solute concentration in the liquid phase. The presence of miscibility gap is investigated in terms of two minima in the free energy curve and the hysteresis in chemical potential curve as a function of solute concentration.

5. The crystal-melt interfacial stiffness is computed from Molecular Dynamics simulations utilizing the CFM analysis of equilibrium height fluctuation of crystal-melt interfaces for different orientations as a function of temperature.

6. The magnitudes and anisotropies of the solid-liquid interface free energy (γ) of Al-Mg system are calculated from the interfacial stiffnesses. Orientationally averaged interfacial energies are examined in detail where the values of γ_0 are observed to show an increasing trend with increasing temperature (decreasing concentration of lower T_M materials) which is in agreement with that results of LJ[75] and HS[32] systems.

7. The temperature dependent solute adsorption coefficient Γ_{Mg}^{Al} is calculated to estimate the relative contribution from interfacial adsorption and excess entropy, S_{xs}, to

interfacial free energy, $\gamma_o(T)$, on the basis of Gibbs adsorption theorem. $\gamma_o(T)$ of binary Al-Mg alloy is found to be largely dominated by the interfacial excess entropy contribution which is consistent with that result of LJ binary system[75] and the crystal-melt interface theory of Spaepen[84].

8. At all temperatures studied, the inequality of the surface energy, γ, due to the orientation dependence follows the trend $\gamma_{100} > \gamma_{110} > \gamma_{111}$ which is consistent with several MD results for elemental fcc system.

9. The anisotropies of interfacial energy of Al-Mg binary alloys are analyzed in detail to investigate the effect of solute concentrations on the anisotropic parameters ε_1 and ε_2. The superimposition of composition dependent ε_1 and ε_2 on the dendrite orientation selection map, proposed by Haxhimali et al.[33], shows the variation of both parameters by a considerable amount with respect to change in the solute content of the system.

10. The location of anisotropic parameters ε_1 and ε_2 in the (ε_1 - ε_2) indicates that the orientation of the primary dendrite growth for pure Al would be in <100> direction. The trend of change in ε_1 and ε_2 in that space predicts that the growth will tend to stabilize in <100> direction with the addition of Mg to the system i.e. for the more concentrated alloys as well.

11. The kinetic coefficient (μ) of pure Al has been computed for both (100) and (110) oriented interfaces from layered free solidification technique using multiple thermostat and fluctuation analysis with a correction due to thermally controlled

kinetics. The magnitudes of interfacial mobility from these computational techniques are found to be equivalent considering the uncertainties for both orientations which can be summarized as follows:

Layered free solidification, $\mu_{100} = 163 \pm 15$ cm/s/K

$$\mu_{110} = 129 \pm 16 \text{ cm/s/K}$$

Corrected fluctuation analysis, $\mu_{100} = 191 \pm 30$ cm/s/K

$$\mu_{110} = 140 \pm 23 \text{ cm/s/K}$$

12. Two aspects of the kinetic coefficient results of pure Al from this work are observed to be consistent with several previous MD studies. First, the inequality of anisotropic μ values follows the trend $\mu_{100} > \mu_{110}$ and the ratio μ_{100}/μ_{110} is found to be in the range of around 1.3 to 1.4 with the error bars.

CHAPTER 7

Future Work

As a consequence of the detailed study of Al-rich Al-Mg alloy in this research project, some suggestions can be summarized for the future work which are as follows:

1. To develop an Al-Mg interatomic potential for the simulation of solid-liquid system of Mg-rich Al-Mg alloys.
2. To reproduce the Mg-rich side of the real Al-Mg phase diagram for the optimization of the new potential.
3. To compute the interface free energy and its associated anisotropy as a function of solute concentration for the Mg-rich Al-Mg binary alloys.
4. To predict the dendrite growth direction of pure Mg and the possible change in the orientation with the addition of Al in the system.
5. To determine the interfacial mobility of pure Mg for different orientations.

References

1. http://www.autoaluminum.org/main/publications-for-download/publications-for-download
2. http://www.autoaluminum.org/main/aluminum-processes-and-materials/aluminum-processes-and-materials
3. http://photography.nationalgeographic.com/staticfiles/NGS/Shared/StaticFiles/Photography/Images/Content/dendrite-snowflake-1047254-sw.jpg
4. J. S. Langer, in *Les Houches, Session XLVI, 1986 – Chance and Matter*, edited by J. Souletie, R. Stora, & J. Vannimenus (Elsevier Science Publishers, North-Holland, Amsterdam, 1987), 629.
5. A. Berbieri & J. S. Langer, *Phys. Rev. A.*, **39**, 5314 (1989).
6. D. Kessler, J. Koplik & H. Levine, *Adv. Phys.*, **37**, 255, (1988).
7. M. Ben Amar & E. Brener, *Phys. Rev. Lett.*, **71**, 589 (1993).
8. A. Karma & W. J. Rappel, *Phys. Rev. Lett.*, **77**, 4050 (1996).
9. A. Karma & W. J. Rappel, *Phys. Rev. E.*, **57**, 4323 (1998).
10. A. Karma, *Phase field methods*, in: K. H. J. Buschow, R. W. Cahn, M. C. Flemings, B. Ilschner, E. J. Cramer & S. Mahajan (Eds.), *Encyclopaedia of Materials: Science and Technology*, **7**, Elsevier, Oxford, 6873 (2001).
11. M. Plapp & A. Karma, *Phys. Rev. Lett.*, **84**, 1740 (2000).
12. M. Plapp & A. Karma, *J. Comp. Phys.*, **165**, 592 (2000).
13. N. Provatas, N. Goldenfeld & J. Dantzig, *Phys. Rev. Lett.*, **80**, 3308 (1998).

14. J. Bragard, A. Karma, Y. H. Lee & M. Plapp, *Interface Sci.*, **10**, 121 (2002).

15. J. J. Hoyt, M. Asta & A. Karma, *Interface Sci.*, **10**, 181 (2002).

16. J. B. Collins, H. Levine, *Phys. Rev. B.*, **31**, 6119 (1985).

17. J. S. Langer, in: G. Grinstein, G. Mazenko (Eds.), *Directions in Condensed Matter*, World Scientific, Singapore, 164 (1986).

18. W. J. Bottinger, J.A. L. Warren, C. Beckermann & A. Karma, *Annu. Rev. Mater. Res.*, **32**, 163 (2002).

19. J. J. Hoyt, M. Asta & A. Karma, *Mater. Sci. Eng. R*, **41**, p. 121 (2002).

20. J. J. Hoyt, M. Asta & A. Karma, *Phys. Rev. Lett.*, **86**, p. 5530 (2001).

21. J. J. Hoyt & M. Asta, *Phys. Rev. B*, **65**, 214106 (2002).

22. M. Asta, J. J. Hoyt & A. Karma, *Phys. Rev. B*, **66**, 100101 (2002).

23. D. Y. Sun, M. Asta, J. J. Hoyt, M. I. Mendelev & D. J. Srolovitz, *Phys. Rev. B*, **69**, p. 020102 (R) (2004).

24. D. Y. Sun, M. Asta & J. J. Hoyt, *Phys. Rev. B*, **69**, p. 174103 (2004).

25. D. Y. Sun, M. Asta & J. J. Hoyt, *Phys. Rev. B*, **69**, p. 024108 (2004).

26. J. R. Morris, *Phys. Rev. B*, **66**, 144104 (2002).

27. D. Y. Sun et al., *Phys. Rev. B*, **73**, 024116 (2006).

28. S. Liu, R. E. Napolitano & R. Trivedi, *Acta Mater.*, **49**, 4271 (2001).

29. R. E. Napolitano, S. Liu & R. Trivedi, *Interf. Sci.*, **10**, 217 (2002).

30. J. R. Morris, *Phys. Rev. B*, **66**, 144104 (2002).

31. C. A. Becker, D. Olmsted, M. Asta, J. J. Hoyt & M. Foiles, *Phys. Rev. Lett.*, **98**, 125701 (2007).

32. M. Amini & B. B. Laird, *Phys. Rev. B*, **78**, 144112 (2008).

33. T. Haxihimali, A. Karma, F. Gonzales & M. Rappaz, *Nature Materials,* **5**, 660 (2006).

34. S. -K. Chan, H. -H. Reimer & M. Kahlweit, *J. Cryst. Growth,* **32**, 303 (1976).

35. K. Pettersen, O. Lohne & M. Ryum, *Metall. Trans. A*, **21**, 221 (1990).

36. S. Henry, P. Jarry, P. -H. Jouneau & M. Rappaz, *Metall. Mater. Trans. A*, **28**, 207 (1997).

37. S. Henry, P. Jarry, P. -H. Jouneau & M. Rappaz, *Metall. Mater. Trans. A*, **29**, 2807 (1998).

38. S. Henry, T. Minghetti & M. Rappaz, *Acta Mater.*, **46**, 6431 (1998).

39. A. Semoroz, Y. Durandet & M. Rappaz, *Acta Mater.*, **49**, 529 (2001).

40. M. I. Mendelev, M. Asta, M. J. Rahman & J. J. Hoyt, *Development of Interatomic Potentials Appropriate for Simulation of Solid-Liquid Interface Properties in Al-Mg Alloys*, accepted to be published in *Phil. Mag.*

41. http://www.ctcms.nist.gov/potentials/

42. H. Ramalingham, M. Asta, A. van de Walle & J. J. Hoyt, *Interface Science*, **10**, 149 (2002).

43. J.J. Hoyt, J.W. Garvin, E.B. Webb III & M. Asta, *Modelling Simul. Mater. Sci. Eng.*, **11**, 287 (2003).

44. C.A. Becker, M. Asta, J.J. Hoyt & S.M. Foiles, *J. Chem. Phys.*, **124**, 164708 (2006).

45. J.R. Morris, C.Z. Wang, K.M. Ho & C.T. Chan, *Phys. Rev. B.*, **49**, 3109 (1994).

46. J.R. Morris & X. Song, *J. Chem. Phys.*, **116**, 9352 (2002).

47. D. Frenkel, *Advanced Monte Carlo Techniques* NATO ASI Series C, vol **397**, ed M.P. Allen & D.J. Tildesley (Dordrect: Kluwer), p 93 (1993).

48. D. Frenkel & B. Smit, *Understanding Molecular Simulation* (New York: Academic) (1996).

49. Y. Zuo & Y.A. Chang, *Calphad-Computer Coupling of Phase Diagrams and Thermochemistry*, **17**, 161 (1993).

50. G.R. Belton & Y.K. Rao, *Transactions of the Metallurgical Society of Aim*, **245**, 2189 (1969).

51. J.M. Juneja, K.P. Abraham & G.N.K. Iyengar, *Scripta Metallurgica*, **20**, 177(1986).

52. R.R. Hultgren, P.D. Desai, D.T. Hawkins et al. *Selected values of the thermodynamic properties of binary alloys.* American Society for Metals, Metals Park, Ohio, 1973.

53. N. Saunders, *CALPHAD*, **14**, 61 (1990).

54. J. L. Murray, *Bulletin of Alloy Phase Diagram*, **3**, 60 (1982).

55. E. Schurmann & I. K. Geissler, *Giessereiforschung*, **32**, 167 (1980).

56. E. Schurmann & H. J. Voss, *Giessereiforschung*, **33**, 43 (1981).

57. W. J. Bottinger, S. R. Coriell, A. L. Greer, A. Karma, W. Kurz, M. Rappaz & R. Trivedi, *Acta Mater.*, **48**, 43 (2000).

58. W. J. Bottinger, J.A. L. Warren, C. Beckermann & A. Karma, *Annu. Rev. Mater. Res.*, **32**, 163 (2002).

59. W.A. Tiller, *The Science of Crystallization: Microscopic Interfacial Phenomena*, Cambridge University Press, New York, 1991.

60. D. P. Woodruff, *The Solid-Liquid Interface*, Cambridge University Press, London (1973).

61. D. Turnbull, *J. Appl. Phys.*, **21**, 1022 (1950).

62. D.R.H. Jones, *J. Mater. Sci.*, **9**, 1 (1974).

63. M.E. Glicksman & N.B. Singh, *J. Cryst. Growth*, **98**, 277 (1989).

64. M. Muschol, D. Liu & H.Z. Cummins, *Phys. Rev. A*, **46**, 1038 (1992).

65. S. Liu, R. E. Napolitano & R. Trivedi, *Acta Mater.*, **49**, 4271 (2001).

66. R. E. Napolitano, S. Liu & R. Trivedi, *Interface Sci.*, **10**, 217 (2002).

67. R. E. Napolitano, S. Liu, *Phys. Rev. B*, **70**, 214103 (2004).

68. G. Wulff, Z. Krist., **34**, 449 (1901).

69. J.Q. Broughton & G.H. Gilmer, *J. Chem. Phys.*, **84**, 5759 (1986).

70. R.L. Davidchack & B.B. Laird, *Phys. Rev. Lett.*, **85**, 4751 (2000).

71. R.L. Davidchack & B.B. Laird, J. Chem. Phys., *J. Chem. Phys.*, **118**, 7651 (2003).

72. R.L. Davidchack & B.B. Laird, *Phys. Rev. Lett.*, **94**, 086102 (2005).

73. Y. Mu, A. Houk & X. Y. Song, *J. Phys. Chem.*, **109**, 6500 (2005).

74. J.R. Morris & X.Y. Song, *J. Chem. Phys.*, **119**, 3920 (2003).

75. C. A. Becker, D. L. Olmsted, M. Asta, J. J. Hoyt & M. Foiles, *Phys. Rev. B,* **79**, 054109 (2009).

76. W. R. Fehlner & S. H. Vosko, *Can. J. Phys.*, **54**, 2159 (1976).

77. S. M. Foiles & J. J. Hoyt, *Acta Mater.*, **54**, 5531 (2006).

78. S. J. Plimpton, *J. Comp. Phys.*, **117**, 1 (1995).

79. http://lammps.sandia.gov/

80. C. A. Becker, *From atoms to dendrites: The properties of alloy crystal-melt interfaces from atomistic simulations*, PhD dissertation, Northwestern University.

81. J. R. Morris, M. I. Mendelev & D. J. Srolovitz, *Journal of Non-Crystalline Solids*, **353**, 3565 (2007).

82. K. F. Kelton, *Solid State Physics*, **45**, 75 (1991).

83. C. H. P. Lupis, *Chemical Thermodynamics of Materials* (Elsevier, New York, 1983).

84. F. Spaepen, *Acta Metall.*, **23**, 729 (1975).

85. S. Henry, P. Jarry, P. -H. Jouneau & M. Rappaz, *Metall. Mater. Trans. A*, **29**, 2807 (1998).

86. S. Henry, T. Minghetti & M. Rappaz, *Acta Mater.*, **46**, 6431 (1998).

87. G. –U. Grun & W. Schneider, in *Light Metals '97*, R. Hulgen, ed., TMS, Warrendale, PA, 1059 (1997).

88. S. Henry, G. –U. Gruen & M. Rappaz, *Metall. Mater. Trans. A*, **35A**, 2495 (2004).

89. R. Willnecker, D.M. Herlach & B. Feuerbacher, *Phys. Rev. Lett.*, **62**, 2707 (1989).

90. J.W. Lum, D.M. Matson & M.C. Flemings, *Metall. Mater. Trans. B*, **27B**, 865 (1996).

91. K. Eckler, F. Gartner, H. Assadi, A.F. Normann, A.L. Greer & D.M. Herlach, *Mater. Sci. Eng.*, A **226-228**, 410 (1997).

92. D.M. Matson, in *Solidification 1998*, edited by S.P. Marsh, J.A. Dantzig, R. Trivedi, W. Hofmeister, M.G. Chu, E.J. Lavernia & J.-H. Chun (The Mineral, Metal and Materials Society, Warrendale, PA, 1998), p. 233.

93. W.J. Boettinger, S.R. Coriell, A.L. Greer, A. Karma, W. Kurz, M. Rappaz & R. Trivedi, *Acta Mater.*, **48**, 43 (2000).

94. J. Bragard, A. Karma, Y.H. Lee & M. Plapp, *Interface Sci.*, **10**, 121 (2002).

95. M.E. Glicksman & R.J. Shaefer, J. Cryst. Growth, **1**, 297 (1967).

96. G.H. Roadway & J.D. Hunt, J. Cryst. Growth, **112**, 554 (1991).

97. J.Q. Broughton, G.H. Gilmer, K.A. Jackson, *Phys. Rev Lett.,* **49**, 1496 (1982).

98. E. Burke, J.Q. Broughton & G.H. Gilmer, *J. Phys. Chem.*, **89**, 1030 (1988).

99. C.J. Tymezak & J.R. Ray, *Phys. Rev. Lett.*, **64**, 1278 (1990).

100. C.J. Tymezak & J.R. Ray, *J. Chem. Phys.*, **92**, 7520 (1990).

101. C.F. Richardson & P. Clancy, *Mol. Simul.*, **7**, 335 (1991).

102. C.F. Richardson & P. Clancy, *Phys. Rev. B*, **45**, 12, 260 (1992).

103. R. Moss & P. Harrowell, *J. Chem. Phys.*, **100**, 7630 (1994).

104. W.J. Briels & H.L. Tepper, *Phys. Rev. Lett.*, **79**, 5074 (1997).

105. H.E.A. Huitema, M.J. Vlot & J.P. van der Eerden, *J. Chem. Phys.*, **111**, 4714 (1999).

106. H.E.A. Huitema, B. van Hengstum & J.P. van der Eerden, *J. Chem. Phys.*, **111**, 10248 (1999).

107. J.J. Hoyt, B. Sadigh, M. Asta, S.M. Foiles, *Acta Mater.*, **47**, 3181 (1999).

108. H.L. Tepper & W.J. Briels, *J. Cryst. Growth*, **230**, 270 (2001).

109. H.L. Tepper & W.J. Briels, *J. Chem. Phys.*, **115**, 9434 (2001).

110. H.L. Tepper & W.J. Briels, *J. Chem. Phys.*, **116**, 5186 (2002).

111. F. Celetini & J.-M. Debierre, *Phys. Rev. E*, **65**, 041605 (2002).

112. K.A. Jackson, *Interface Sci.*, **10**, 159 (2002).

113. J.J. Hoyt, M. Asta & D.Y. Sun, *Philos. Mag.*, **86**, 3651 (2006).

114. M. Amini & B.B. Laird, *Phys. Rev. Lett.*, **97**, 216102 (2006).

115. Z.G. Xia, D.Y. Sun, M. Asta & J.J. Hoyt, *Phys. Rev. B*, **75**, 012103 (2007).

116. K.A. Jackson & B. Chalmers, *Can. J. Phys.*, **34**, 473 (1956).

117. H.A. Wilson, *Philos. Mag.*, **50**, 238 (1900).

118. J. Frenkel, *Phys. Z. Sowjetunion*, **1**, 498 (1932).

119. D. Turnbull & B.G. Bagley, *Solid State Chem.*, **5**, 526 (1975).

120. S.R. Coriell & D. Turnbull, *Acta Metall.*, **30**, 2135 (1982).

121. L.V. Mikheev, A.A. Chernov, *J. Cryst. Growth,* **112**, 591 (1991).

122. J. Monk, Y. Yang, M.I. Mendelev, M. Asta, J.J. Hoyt & D.Y. Sun, *Determination of Kinetic Coefficient from Molecular Dynamics Simulations*.

123. A. Karma, *Phys. Rev. E*, **48**, 3441 (1993).

124. F. Muller-Plathe & D. Reith, *Comp. Theor. Polym. Sci.*, **9**, 203 (1999).

125. F. Muller-Plathe, *J. Chem. Phys.*, **106** (14), 6082 (1997).